공학박사학위논문

파티클 시뮬레이션을 이용한 물리 기반 비강체 정합 기술

Physically based Non-rigid Registration using Smoothed Particle Hydrodynamics

2013년 8월

서울대학교 대학원
전기컴퓨터공학부
표순형

파티클 시뮬레이션을 이용한 물리 기반 비강체 정합 기술

Physically based Non-rigid Registration using Smoothed Particle Hydrodynamics

지도 교수 신영길

이 논문을 공학박사 학위논문으로 제출함
2013년 4월

서울대학교 대학원
전기컴퓨터공학부
표순형

표순형의 박사 학위논문을 인준함
2013년 6월

위 원 장	이제희	(인)
부위원장	신영길	(인)
위 원	서진욱	(인)
위 원	김보형	(인)
위 원	이정진	(인)

Abstract

Recent advances in computing hardware have enabled the application of physically based simulation techniques to various research fields for improved accuracy. In this paper, we present a novel physically based non-rigid registration method using smoothed particle hydrodynamics (SPH) for hepatic metastasis volume-preserving registration between follow-up liver CT images. Our method models the liver and hepatic metastasis as a set of particles carrying their own physical properties. Based on the fact that the hepatic metastasis is stiffer than other normal cells in the liver parenchyma, the candidate regions of hepatic metastasis are modeled with particles of higher stiffness compared to the liver parenchyma. Particles placed in the liver and candidate regions of hepatic metastasis in the source image are transformed along a gradient vector flow (GVF)-based force field calculated in the target image. In this transformation, the particles are physically interacted and deformed by a novel deformable particle method which is proposed to preserve the hepatic metastasis to the best. In experimental results using 10 clinical datasets, our method matches the liver effectively between follow-up CT images as well as preserves the volume of hepatic metastasis almost completely, enabling the accurate assessment of the volume change of the hepatic metastasis. These results demonstrated a potential of the proposed method that it can deliver a substantial aid in measuring the size change of index lesion (i.e., hepatic metastasis) after the chemotheraphy of metastasis patients in radiation oncology.

Keywords: Computed tomography (CT), Hepatic metastasis, Volume-preserving particle method, Computer simulation, Smoothed particle hydrodynamics

Student Number: 99325-811

Contents

List of Figures

List of Tables

Chapter 1

Introduction

1.1 Motivation

Computed tomography (CT) is a well-established means of diagnosing hepatic metastases (hereinafter, metastases) in patients with metastatic liver disease and of evaluating the progression and regression of liver disease during treatment [3]. Using advanced multislice CT scanners, the sensitivity for the detection of metastasis has greatly improved. In addition, CT has found its increasing usage in the liver cancer screening for high-risk individuals, showing very promising results for identifying early-stage liver cancer [4]. Using sequential follow-up CT scans, radiologists or oncologists want to assess the change in size and number of metastases [4]. For the accurate assessment of the change of metastases, the registration of the liver between follow-up CT scans is essential that supports the direct comparison of the changing metastasis in the same geometric condition.

The follow-up CT images are usually obtained with some time interval. The liver in a follow-up CT scan thus differs greatly in shape from that in a reference CT scan due to the movement of a patient and/or the respiratory and heart motions. Such shape difference makes it hard to find an accurate solution for the liver registration. Furthermore, it has been shown that cancers in an organ are stiffer than the normal tissue of that organ [5, 6, 7]. That means that the metastasis and the normal liver tissue should exhibit different resistance to the change during the registration. One thing to be noted in the liver registration is that the volume of the metastasis should be preserved during the registration. Therefore, a physically based registration method, which can preserve the volume of metastasis while considering the spatially varying physical properties of the liver (e.g. difference in stiffness for cancer and normal tissue), is a successful solution to the liver registration.

Several approaches that automatically register follow-up liver CT images have been proposed. Charnoz *et al.* [8, 9] proposed a follow-up liver registration method using a tree matching technique. First, portal veins are segmented from each CT image, and modeled as trees using skeletonization. Then, common bifurcations and edges between them are matched and their deformations are extrapolated to estimate local deformations inside the liver. However, the region far from the main vascular structures cannot be accurately deformed since the method only uses the registered information of the main vascular structures. Okumura *et al.* [10] proposed a registration method to align the automatically segmented liver shape between follow-up CT images. This method binarized the segmented liver to have an intensity value of 1, and performed the registration to minimize the intensity difference between these binarized images of follow-up CT images. They proved the usefulness of the method for their tested datasets in performing the growth assessment of small hepatocellular carcinomas. However, they used x- and y-axes translation only (i.e., 2D registration), so they might not perform successfully for the datasets which require a 3D registration. Fujioka *et al.* [11] proposed the registration method between pre- and post-operative CT images to evaluate the therapeutic response for the radiofrequency ablation (RFA) of hepatocellular carcinoma. First, rigid registration is performed using the similarity measure based on the normalized correlation coefficient. Then, manual registration for the fine adjustment is performed using the manually defined hepatic margin and portal veins near the tumor. Therefore, it requires a lot of manual interventions when the liver shape is quite different between pre- and post-RFA CT images. All the approaches described above [8, 9, 10, 11] are basically based on the intensity information of CT images. To the best of our knowledge, there has been no physically based approach for the registration of follow-up liver CT images.

1.2 Dissertation Goals

In this dissertation, we propose a novel physically based non-rigid registration method using smoothed particle hydrodynamics (SPH) for metastasis volume-preserving registration between follow-up CT images. Our method models the liver and metastasis, which are both automatically detected in a preprocessing step, as a set of particles carrying their own physical properties. Based on the fact that the metastasis is stiffer than other normal cells in the liver parenchyma, the candidate regions of metastasis are modeled with particles of higher stiffness compared to the liver parenchyma. Particles are placed in the liver and candidate regions of metastasis in the source floating image, and a gradient vector flow (GVF)-based force field is generated in the target reference image. And then, the particles are physically interacted and deformed using a novel deformable particle method which is proposed to preserve the metastasis to the best. In this way, our method matches the liver successfully between follow-up CT images while preserving the volume of metastasis very well.

1.3 Main Contribution

The purpose of this study is to develop a physically based non-rigid registration method which preserves the volume of hepatic metastasis through the registration process. To physically deform a given shape to a target shape while preserving its volume, a new particle based deformable simulation method is proposed. Since existing methods allow overlap of particles to compute elastic force between them from the difference in relative positions, severe volume change could be aroused when big external force is applied to the shape. Meanwhile, the proposed method keeps the shape's volume preserved by letting each particle's volume preserved. When external force makes two particles overlap, the particles are scaled down in the direction of overlap and expanded in other directions to make its volume constant. The proposed method was applied to register livers in follow-up CT images and improved the registration accuracy while minimizing volume change of candidate regions of hepatic metastasis.

1.4 Organization of the Dissertation

The remainder of this paper is organized as follows. The Chapter 2 gives a brief overview of image registration and smoothed particle hydrodynamics and presents related works. The next chapter describes deformable particle method after introducing SPH methods used for the simulation of deformable objects. Then, the proposed method of physically based non-rigid registration using SPH is described in Chapter 4. In Chapter 5, the overall workflow of the proposed algorithm and some issues on implementation of it are described. Chapter 6 presents the results of the application of the proposed method to clinical datasets along with a comparison to a couple of previous methods. Finally, we summarize the results and discuss future work in Chapter 7.

Chapter 2

Background

2.1 Medical Image Registration

Image registration is the process of transforming a source (floating) image to be in the same coordinate system with a target (reference) image. The images may be from different sensors, from different times, or from different viewpoints. When the images are from medical imaging devices, it is called medical image registration. Medical image registration plays an increasingly important role in many clinical applications, including the detection and diagnosis of diseases, planning therapy, guidance of interventions, and follow-up and monitoring of patients [12].

The medical images are usually acquired using computed tomography (CT), magnetic resonance imaging (MRI), positron emission tomography (PET), and ultrasound imaging devices. The registration methods can be classified by the types of modalities used for the source and target images. In monomodal applications, the images to be registered belong to the same modality, as opposed to multimodal registration, where the images to be registered stem from two different modalities. Examples of multimodal regis-

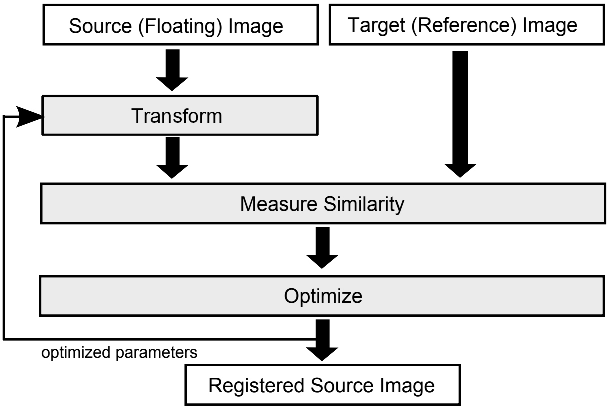

Figure 1: General process of medical image registration

tration include registration of brain CT/MRI images or whole body PET/CT images for tumor localization and registration of contrast-enhanced CT images against non-contrast-enhanced CT images for segmentation of specific parts of the anatomy. Another classification can be made between intra-subject and inter-subject. A method is intra-subject if both images are from the same patient, but otherwise, it is inter-subject. The inter-subject registration is commonly used to study the anatomical variability within or across populations.

The image registration process is finding optimal geometric transformation that maximizes the correspondences across the images. In general, the process is comprised of three main components as shown in Figure 1: Transformation models to deform the source image, similarity metrics to measure the correspondence between the source and target images, and optimization methods to maximize the correspondence. A source image is deformed to a transformed source image and it is compared with a target image to measure similarity between them. Unless the correspondence is enough to meet the metric, parameters for the transform is optimized and the steps are repeated. The deformed source image which meets the metric is produced as the final result. In following sections, we will shortly review previous works on these components and provide related works on physically based registration at the end.

2.1.1 Transformation Models

A transformation model in image registration defines a geometric transformation $\mathbf{T} : (x,y,z) \rightarrow (x',y',z')$, which maps any point in the source image into the corresponding point in the target image. The transformation models can be classified into transformations for rigid registration and transformations for non-rigid registration as shown in Figure 2. Rigid registration globally aligns a source image to a target image by applying a transformation to entire image domain. In contrast to rigid registration, non-rigid registration aligns a source image to a target image by locally warping the source image. The non-rigid transformations can be modeled either using parametric or non-parametric models. In the case of non-parametric transformation models, a dense displacement field is stored which describes the

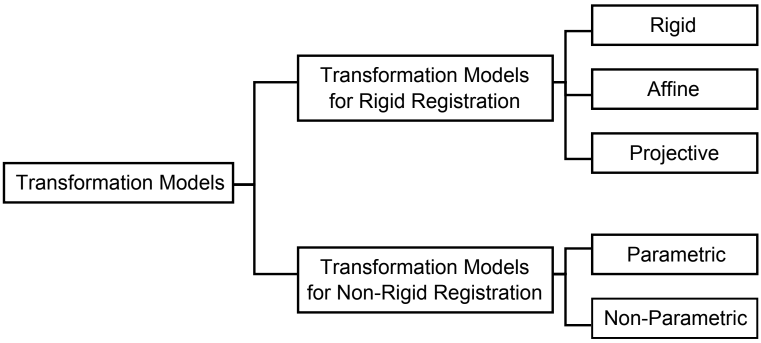

Figure 2: Taxonomy of transformation models for image registration.

deformation at every voxles. In contrast to this, parametric transformation models are controlled by a set of parameters. Some typical transformation models in each category will be summarized in following subsections. For the full review of these models, please refer to [13, 14, 15].

Transformations for Rigid Registration

The simplest but most widely used transformation model is rigid transformation. It is appropriate for anatomical structure like skull or bone since it is rigid and constrains the motion of content inside sufficiently. A rigid transformation does not alter the size or shape of an image, but translates and rotates it preserving relative distances of any two points in the image. The rigid transformation is given by

$$\mathbf{T}_{rigid}(\mathbf{x}) = \mathbf{R}(\mathbf{x}) + \mathbf{t} \tag{2.1}$$

where **x** is a position vector, **t** is a translation vector along axes of the coordinate system, and **R** is a rotation matrix which is the multiplication of three separate rotation matrices about each coordinate axis. In three dimensions, a rigid transformation involves six degrees of freedom. In some cases, it is necessary to correct not only for rigid transformation but also for scaling and shears caused by the gantry tilt of CT scanners. Combining the rigid transformation matrix with the scaling and shearing matrices yields an affine transformation

$$\mathbf{T}_{affine}(\mathbf{x}) = \mathbf{T}_{shear} \cdot \mathbf{T}_{scale} \cdot \mathbf{T}_{rigid}(\mathbf{x}) \tag{2.2}$$

whose twelve degrees of freedom represent rotations, translations, scaling and shears. The affine transformation changes the size and shape of an image, but it preserves the parallelism of lines in the image. Since the rigid and affine transformations affect the entire image domain, they are sometimes called global transformation. Projective transformation is also sometimes used to align 3D volumes like CT or MRI to 2D images such as radiography and photography. Since it could be reduced to rigid transformation using camera calibration technique [16], it will not be explained further here. Figure 3 shows examples of each transformation. Figure 3(a) is an original image before applying any transformation to it and Figure 3(b) is an exam-

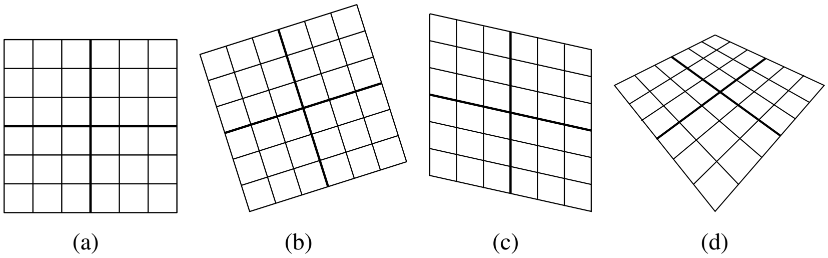

Figure 3: Examples of transformations for rigid registration. (a) is an original source image and (b), (c), and (d) show images deformed by using rigid transformation, affine transformation, and perspective transformation, respectively.

ple image which is deformed by applying the rigid transformation to Figure 3(a). It is deformed only by translation and rotation. Figure 3(c) shows an example image deformed by the affine transformation and it is scaled and sheared besides being rotated and translated. In this case, the parallelism of lines is preserved after transformation. Figure 3(d) is obtained by applying the projective transformation to Figure 3(a). It can be seen that the lines are not parallel anymore.

Non-Rigid Transformation: Parametric Models

While the transformation models discussed so far can be used for the registration of rigid anatomical structures like the skull and bones, they are not applicable to the soft tissues which deforms significantly. Registration of soft tissues like the liver and breast requires deformable or non-rigid transformations. In the case of non-rigid registration, it is common to optimize a spatially varying displacement field u to express the transformation, i.e., $\mathbf{T}(\mathbf{x}) = \mathbf{x} + \mathbf{u}(\mathbf{x})$.

The typical non-rigid transformation model is parametric transformation model which describes the transformation as a linear combination of basis functions. One of this approach is the spline-based transformation model. A common assumption in this model is that a set of corresponding points or landmarks can be identified in the source and target images. These corresponding points are often referred to as control points. At these control points, spline-based transforms either interpolate or approximate the displacements, which are necessary to map the locations of corresponding control points in both images. The spline-based transformation provides smoothly varying displacement fields for the pixels or voxels between control points. The most widely used spline-based model for image registration is thin-plate spline (TPS) method which was originally proposed by Duchon [17] and Meiguet [18] for the surface interpolation of scattered data. Given a set of corresponding sets of control points or landmarks, the spline coefficients can be determined by the method of least square [19]. In 2D, the thin plate spline has a logarithmic basis function $r^2 \log(r)$, in 3D this simplifies to r [20]. So the displacement $u(\mathbf{x})$ can be determined as follows [21]:

$$\mathbf{u}(\mathbf{x}) = \mathbf{A}\mathbf{x} + \mathbf{B} + \mathbf{I}\sum_{i=1}^{N} F_i r_i^2 \log(r_i) \tag{2.3}$$

$$\mathbf{u}(\mathbf{x}) = \mathbf{A}\mathbf{x} + \mathbf{B} + \mathbf{I}\sum_{i=1}^{N} F_i r_i \tag{2.4}$$

where (2.3) and (2.4) refer to 2D and 3D space respectively. The matrices **A** and **B** define an affine transformation and **I** is the identity matrix. The coefficients of the linear transform defined by **A** and **B** and the thin-plate spline coefficients F_i are determined by solving the set of linear equations at the locations of landmarks in the source image. Since the thin-plate spline is a global supported function, it cannot accurately model localized deformation. Furthermore, outliers have a global impact and large deformations can lead to singularities in the sets of equations that need to be solved. This can make the topology not to be preserved through the registration. The global extent also leads to high computational complexity when large numbers of landmarks are used.

In the late 1980s, Free Form Deformation (FFD) method is proposed by Sederberg and Parry in the computer graphics community [22]. The basic idea of FFD is to deform an object by manipulating an underlying mesh of control points and interpolating the deformation between control points using Bernstein polynomials. Later, tri-variate B-spline tensor product became more popular as the deformation function [23, 24] and Rueckert used B-spline based FFD for image registration for the first time [25, 2]. To define a spline-based FFD, let Φ denote a $n_x \times n_y \times n_z$ mesh of control points $\phi_{i,j,k}$ with uniform control point spacing δ. Then, the FFD can be written as the 3D tensor product of the 1D cubic B-splines:

$$\mathbf{T}_{B-spline}(\mathbf{x}) = \sum_{l=0}^{3}\sum_{m=0}^{3}\sum_{n=0}^{3} B_l(u)B_m(u)B_n(w)\phi_{i+l,j+m,k+n} \tag{2.5}$$

where i, j, and k denote the index of the control point cell containing $\mathbf{x} = (x,y,z)$, and u, v, and w are the relative positions of x, y, and z, respectively, inside the cell, e.g., $i = \lfloor \frac{x}{\delta} \rfloor - 1$ and $u = \frac{x}{\delta} - \lfloor \frac{x}{\delta} \rfloor$. The functions B_0 through B_3 are the approximating third-order spline polynomials as described in [24]

$$\begin{aligned}
B_0(u) &= (1-u)^3/6 \\
B_1(u) &= (3u^3 - 6u^2 + 4)/6 \\
B_2(u) &= (-3u^3 + 3u^2 + 3u + 1)/6 \\
B_3(u) &= u^3/6
\end{aligned} \tag{2.6}$$

Since B-splines are locally controlled in contrast to thin-plate splines, they are computationally efficient even for a large number of control points. In particular, the basis functions of cubic B-splines have a limited support and let change of a control point affect the transformation only in the local neighborhood of that point.

Non-Rigid Transformation: Non-Parametric Models

In contrast to parametric transformation models, non-parametric models characterize the deformation at every voxel. These models provide the greatest amount of flexibility in describing the transformation but are also expensive in terms of memory usage. The non-parametric transformation models can be classified into small deformation models in which deformation is stored at each voxel as displacement vectors with respect to their initial positions and large deformation models in which the displacement is generated via a time dependent velocity field $\mathbf{v}$ [15].

The small deformation model usually generates the transformation from the source image to the target image as a physical process, which resembles the stretching of an elastic material such as rubber [26]. The physical process is governed by two forces: The first term is the internal force, which is caused by the deformation of elastic material, i.e., stress and counteracts any force, which deforms the elastic body from its equilibrium state. The second term is the external force which acts on the elastic body from outside. The deformation of the source shape stops if the internal and the external forces acting on the body form an equilibrium solution. The equilibrium state for an isotropic homogeneous body is described by the Navier linear elastic partial differential equation (PDE):

$$\mu\nabla^2\mathbf{u}+(\lambda+\mu)\frac{\partial\theta}{\partial\mathbf{x}}+\mathbf{f}=0 \tag{2.7}$$

where θ is cubical dilation,

$$\theta=\frac{\partial u_1}{\partial x_1}+\frac{\partial u_2}{\partial x_2}+\frac{\partial u_3}{\partial x_3}. \tag{2.8}$$

$\mathbf{x}=(x_1,x_2,x_3)^T$ refers to the coordinate system before deformation, $\mathbf{u}=(u_1,u_2,u_3)^T$ are the displacements we want to find, and $\mathbf{f}=(f_1,f_2,f_3)^T$ are the external forces. Elastic constants μ and λ define the elastic properties of the body and they are often interpreted in terms of Young's modulus E, which relates the strain and stress of an object and Poisson's ratio ν, which is the ratio between lateral shrinking and longitudinal stretching:

$$E=\frac{\mu(3\lambda+2\mu)}{(\lambda+\mu)},\nu=\frac{\lambda}{2(\mu+\lambda)} \tag{2.9}$$

The external force **f** is the force which acts on the elastic body and drives the registration process. A common choice for the external force is the gradient of a similarity measure. The partial differential equation in (2.7) may be solved by finite differences and Successive Over-Relaxation(SOR) and this yields a discrete displacement field for each voxel. An extension of the elastic registration framework has been proposed by Davatzikos [27] to allow for spatially varying elasticity parameters. This enables certain anatomical structures to deform more freely than others.

In the small deformation model, highly localized deformations cannot be modeled since the deformation energy caused by stress increases proportionally with the strength of the deformation. To overcome this limitation, Christensen *et al.* proposed a model in which the displacement is generated via a time dependent velocity field based on fluid dynamics [28]. Here the deformations are characterized by the Navier-Stokes partial differential equation

$$\mu\nabla^2\mathbf{v}(x,y,z)+(\lambda+\mu)\nabla(\nabla\cdot\mathbf{v}(x,y,z))+\mathbf{f}(x,y,z)=0 \tag{2.10}$$

similar to (2.7) except that differentiation is carried out on the velocity field **v** rather than on the displacement file **u** and is solved for each time step. The fluid-based registration no longer seeks to optimize the displacement at each location directly but instead estimates a velocity field that is used to provide the displacement. In this case, the end point of a flow determined by the velocity is the corresponding point of a given point in the source image. The fluid flow based registration method allows large localized deformations to be modeled, but has disadvantage of sometimes increasing registration error and high computational cost [29].

2.1.2 Similarity Metrics

The second component of image registration is similarity metrics that measure the degree of alignment of the source and target images. The two main approaches are feature-based and intensity-based similarity measures. Feature-based approaches usually utilize points, lines, or contours and aim to minimize the distance between corresponding features in the images. Knowing the correspondence between a number of points in images, a transformation is then determined to map the source image to the target images, thereby establishing point-by-point correspondence between the source and target images. Since these approaches are based on the geometric features instead of the intensity values in the images, these can be applied to both mono- and multimodality registrations. However, a preprocessing stage to extract the features is needed and any error during the feature extraction will adversely affect the registration and cannot be recovered at a later stage. In contrast to the feature-based approaches, the intensity-based approaches compare intensity patterns in the image via correlation metrics avoiding such errors. This is relatively simple but using image intensities makes it hard to be applicable to multimodality registration. However, its robustness and accuracy made it become the method of choice for measuring image alignment over the last decades. Here, we will summarize some popular voxel-based similarity measures.

Sum of Squared Intensity Differences

The simplest statistical measure of image similarity is based on the sum of squared intensity differences (SSD) between images I_A and I_B,

$$SSD = -\frac{1}{n}\sum (I_A(\mathbf{x}) - I_B(\mathbf{T}(\mathbf{x})))^2, \tag{2.11}$$

where $\mathbf{x}$ is a point in image I_A, $\mathbf{T}(\mathbf{x})$ is the corresponding location in I_B and n is the number of voxels in the overlap region. If the images are correctly aligned, the difference between them should be zero except for noises, and the SSD measure can be shown to be optimal if the noise is Gaussian. This measure is widely used for mono-modality registration in which both images show same range of intensities for the same anatomical structures. However, this method is very sensitive to outlier voxels caused by presence of additional information in one image and the assumption of identical imaging modality can be too restrictive to be used for general purpose.

Normalized Cross Correlation

Normalized cross correlation (NCC) is more robust measure which can be used when there is a linear relationship between intensity values in images I_A and I_B. The most common form is given by

$$NCC = \frac{\sum (I_A(\mathbf{x}) - \mu_A)(I_B(\mathbf{T}(\mathbf{x})) - \mu_B)}{\sqrt{(\sum I_A(\mathbf{x}) - \mu_A)^2 (\sum I_B(\mathbf{T}(\mathbf{x})) - \mu_B)^2}}, \tag{2.12}$$

where μ_A and μ_B correspond to the average voxel intensities in each image. Both images are best aligned if the NCC value is maximized and this is applicable both in the spatial domain and in the frequency spatial domain. While more flexible than SSD, the application of this similarity measure is nevertheless largely restricted to mono-modal registration tasks. Roche applied NCC to multi-modality images assuming that a function that relates intensities was known [30].

Joint Entropy

There has been significant interest in measures of alignment based on the information content or entropy of the registered images. The *Shannon entropy H* is widely used as a measure of information in many branches of engineering. It was originally developed as part of information theory in the 1940s [31] and weighted the information per outcome by the probability of that outcome occurring. Given events $e_1, \cdots, e_m$ occurring with probabilities $p_1, \cdots, p_m$, the Shannon entropy is defined as

$$H = \sum_i p_i \log \frac{1}{p_i} = -\sum_i p_i \log p_i. \tag{2.13}$$

The term $\log \frac{1}{p_i}$ signifies that the amount of information gained from an event with probability p_i is inversely related to the probability that the event takes place. The more rare an event, the more meaning is assigned to occurrence of the event. The Shannon entropy can be computed for an image, in which case we focus on the distribution of the gray values of the image instead of events. A probability distribution of gray values can be estimated by counting the number of times each gray value occurs in the image and dividing those numbers by the total number of occurrences. An image consisting of a single intensity will have low entropy value since it contains very little information. The joint entropy $H(I_A, I_B)$ of the overlapping region of images I_A and I_B may be defined by

$$H(I_A, I_B) = -\sum_a \sum_b p(a,b) \log p(a,b), \tag{2.14}$$

where $p(a,b)$ is the joint probability that a voxel in the overlapping region of image I_A and I_B has value a and b, respectively. The joint entropy can be used for image registration in the form of joint histogram and probability density functions (PDFs). When the images are correctly aligned, the joint histogram have tight clusters surrounded by large dark regions showing that a small number of events is having high probabilities. As the clusters disperse, the high intensity regions of the joint histogram become less intense and previously dark regions become brighter. Misregistration results in an increase in histogram entropy. Therefore, the joint histogram entropy should be minimized to register two images. For the full review of methods using joint entropy and mutual information described in the next subsection, please refer to [32].

Mutual Information

To quantify image alignment, one can use measures from information theory such as mutual information (MI) [33, 34]. The definition of mutual information is given by

$$I_{MI}(I_A, I_B) = H(I_A) + H(I_B) - H(I_A, I_B). \tag{2.15}$$

This form contains the term $-H(I_A, I_B)$, which means that maximizing mutual information is related to minimizing joint entropy. The advantage of mutual information over joint entropy per se, is that it includes the entropies of the separate images. Mutual information and joint entropy are computed for the overlapping parts of the images and the measures are therefore sensitive to the size and the contents of overlap. A problem that can occur when using joint entropy on its own, is that low values (normally associated with high degree of alignment) can be found for complete misregistrations. For example, when only background region is overlapped, it could be regarded as two images are well aligned. Studholme showed that mutual information also can be affected by the degree of overlap between two images [35]. Studholme and Maes suggested the use of normalized mutual information (NMI) as an alternative measure [35, 33]. It is given by

$$I_{NMI}(I_A, I_B) = \frac{H(I_A) + H(I_B)}{H(I_A, I_B)}. \tag{2.16}$$

2.1.3 Optimization

The image registration process is finding optimal geometric transformation that maximizes the correspondences across the images. In certain special cases, such as the rigid registration of pairs of corresponding landmarks, it is possible to analytically estimate the optimal transformation (in a least squares sense). Such an example is, however, exceptional as the majority of registrations are intensity-based registrations and these typically rely on numerical methods to find the optimal parameters. Many numerical optimization methods have been applied to medical image registration and their comparative evaluation can be found in [36, 37]. Maes *et al.* evaluated various multiresolution gradient- and non-gradient-based optimization strategies, such as Powell, simplex, steepest-descent, conjugate-gradient, quasi-Newton and Levenberg-Marquardt methods, for the rigid registration of images from multimodality with mutual information [36]. More recently, Klein *et al.* evaluated optimization methods for non-rigid registration of medical images using B-spline and mutual information [37].

The problem of image registration can be formulated as an optimization problem whose goal is to maximize an objective function. In general, the objective function can be written as combination of two terms: The first term aims at maximizing the similarity of the images and is the driving force behind the registration process. The second term aims at minimizing the cost associated with particular transformations. In the case of rigid or affine registration, the second term usually plays no role and is often omitted. In this case, maximizing the objective function is equal to maximizing the similarity metric. However, in the case of non-rigid registration, the second term can act as a regularization or penalty function which can be used to constrain the transformation relating both images: For example, in elastic or fluid registration the regularization term (linear-elasticity model) forms an integral part of the registration. The proposed method in this dissertation is an example of the non-rigid registration method which uses a linear-elasticity model.

The difference in geometric shape works as the first similarity term, and the forces between the particles in an object work as the regularization term. In contrast to other registration approaches, the intensity values of the images are not considered as a similarity metric in our case.

2.1.4 Physically Based Non-Rigid Registration

As stated in Section 2.1.1, most non-parametric transformation models are based on physical processes for the registration. As the motion and deformation of human organ is governed by physics by nature, it is quite natural to devise physically based methods for the registration of objects in medical images. Broit [38] pioneered the physically based registration by simulating a model in which one of the images made from an elastic material is deformed until it matches an atlas image of the same anatomy. The cross correlation function which measures the similarity between the two images serves as a potential function from which the forces required to deform the image are derived. The equilibrium state is obtained by solving a set of partial differential equations taken from the linear theory of elasticity. These equations are solved iteratively using the finite differences approximation on a grid which describes the mapping. This workflow has been common in physically based registration methods. The object which needs to be registered is represented as physical material and its deformation is iteratively simulated by solving differential equations which describe physical behavior of the material used. When a cost function is optimized and conditions for a similarity measure is fulfilled, the simulation finishes and deformation fields are generated for the registration. Though physically based approaches provide accurate results to non-rigid registration, it has been known to be very time consuming as discussed in [39]. However, recent advances in computing hardware and numerous speed-up techniques made it possible to be used for many applications including medical surgery simulations [40, 41].

The physically based methods can be classified into two groups according to materials used to represent the deforming objects. The first group regarded the object as fluid-like material and applied fluid dynamics to the deformation [28, 42, 39] and the methods in the other group used elastic material to simulate the shape change [38, 26, 43, 27]. The methods in the second group are based on linear elasticity which restricts the registration to globally smooth and therefore to locally small deformation. In contrast, methods in the first group are based on viscous fluid which able to flow to match the reference image even if large-scale deformations are required. These groups are therefore also classified into large deformation model and small deformation model, respectively. The fluid based methods are very useful for the applications where individual variabilities associated with the shapes of constituent biological structures are relatively big as in the case of human brain-structure while the linear elasticity based methods are useful for the registration of organs with less variabilities in shape.

Bajcsy and Kovačič [26] extended Broit's work by implementing a multiresolution version of the linear elasticity model where the deformation of the source image proceeds step-by-step in a coarse to fine strategy, increasing the local similarity and global coherence. They modeled the template image as a linear elastic solid and deformed it using forces derived from an approximation of the local gradient of a correlation based similarity measure. This was the first to demonstrate volumetric non-rigid registration of medical images. An extension of the elastic registration framework has been proposed by Davatzikos [27] to allow for spatially varying elasticity properties. This enables certain anatomical structures to deform more freely than others. However, highly localized deformations cannot be yet modeled with these elasticity based methods since the deformation energy caused by stress increases proportionally with the strength of the deformation. To overcome the limitation of small deformation in the elasticity model, Christensen *et al.* proposed a model in which the displacement is generated via a time dependent velocity field based on fluid dynamics [28]. The smoothness of displacement is guaranteed without penalizing large-magnitude deformations of small subvolumes by constraining the transformation on the basis of a Stokesian limit of the fluid-dynamical Navier-Stokes equations. The viscous fluid PDE is solved on a discrete lattice and the transformation is evaluated at these spatial grid points. Since the evaluated transformation could become singular over time, regridding of template is used by generating a new template whenever the magnitude of the Jacobian drops below certain value indicating that the discretized transformation is approaching local singularity. Since original implementation of this method is based on successive over-relaxation, it demanded lots of computational cost and thus was time consuming. Bro-Nielsen *et al.* proposed a new algorithm which is based on convolution filter and suggested that its performance results in a speed up of at least an order of magnitude [42]. Later, Wollny *et al.* compared computational performances of these methods [39].

In summary, both linear elasticity and viscous fluid models are commonly used physical models in non-parametric non-rigid image registration. Linear elasticity is appropriate for the registration of images with small local displacements while fluid is for the cases with large deformations such as registration of biological structures with varying in both global and local shape across population. The only obstacles to widespread clinical used of these methods are computational cost and the difficulty in validating the results. However, recent advances in computing hardware will make them expected to be widely used clinically soon.

2.2 Smoothed Particle Hydrodynamics

Recent advances in computing hardware enabled computationally expensive simulation techniques to be used in many research fields. For example, simulation of dynamic systems such as liquids, gases, or elastic materials are being important part of computer graphics for generation of physically plausible animation of natural phenomena. Currently, the most common simulation methods are mesh or grid-based. The mesh-based methods require a predefined mesh connecting the data points in the simulation domain and usually the simulation domain itself is discretized into grids to compute velocities or other information on those grid points. If the grid is fixed on the space, the method is called as Eulerian method while it is called as Lagrangian method when the grid is fixed to or attached on the simulated material. The finite difference method (FDM), finite volume method (FVM), and finite element method (FEM) are examples of the mesh-based method. Conventional mesh-based methods such as FDM and FEM have been widely applied to various areas of computational fluid dynamics, and currently are dominant methods in numerical simulations. Despite its popularity, it is hard to construct a regular grid for complex geometry and the connectivity of the mesh can be difficult to maintain without introducing error into the simulation in the cases where the material being simulated can move around (as in computational fluid dynamics) or where large deformations of the material can occur (as in simulations of plastic materials). To remedy these problems, mesh-free approaches are getting strong intersect recently. The mesh-free methods let the necessary functions and derivatives are interpolated from irregular samples without using any mesh that provides the connectivity of these nodes or particles. Smoothed particle hydrodynamics (SPH) and discrete element method (DEM) are most popular mesh-free approaches. SPH is a function approximation framework which was originally proposed by Gingold and Monaghan [44] and separately by Lucy [45] for modeling astrophysical phenomena, and later widely extended for applications to problems of continuum solid and fluid dynamics. Since the proposed method in this thesis is based on SPH, we will shortly review on SPH in this section. For the full review of SPH, please refer to [46, 47, 48].

2.2.1 Formulation of SPH

SPH is a Lagrangian method that uses an interpolation kernel of compact support to represent any field quantity in terms of its values at a set of disordered points (e.g., particles). The simulated material is discretized to elements, and the properties of each element are associated with its center, which is then interpreted as a particle.

Any function $A(\mathbf{x})$ can be rewritten as a convolution

$$A(\mathbf{x}) = \int A(\mathbf{x}')\delta(\mathbf{x}-\mathbf{x}')\mathbf{dV}, \tag{2.17}$$

where δ is the Dirac-delta function. Since $A(\mathbf{x})$ cannot be evaluated everywhere, the Dirac-delta function is replaced with a kernel function W:

$$A_I(\mathbf{x}) = \int A(\mathbf{x}')W(\mathbf{x}-\mathbf{x}',h)\mathbf{dV}, \tag{2.18}$$

where h is the kernel support. Kernels are parametrized with h, allowing control over how far the influence of each same point reaches. The kernel function W has the two properties to reproduce a smoothed function $A(\mathbf{x})$

$$\int W(\mathbf{x}-\mathbf{x}',h)\mathbf{dV} = 1 \tag{2.19}$$

and

$$\lim_{h \to 0} W(\mathbf{x}-\mathbf{x}',h) = \delta(\mathbf{x}-\mathbf{x}'), \tag{2.20}$$

where the limit is to be interpreted as the limit of the corresponding integral interpolants. The integral interpolant can be approximated by a summation interpolant

$$A_S(\mathbf{x}) = \sum_j m_j \frac{A_j}{\rho_j} W(\mathbf{x}-\mathbf{x}_j,h) \tag{2.21}$$

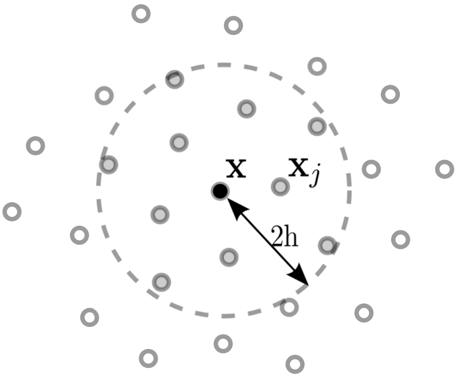

Figure 4: Particle approximations using particles within the kernel support

where A_j, ρ_j and m_j are the value of A, density and mass at position $\mathbf{x}_j$, respectively. The sum is over all particles j within a radius $2h$ of $\mathbf{x}$ as shown in Figure 4. In our method, $W(\mathbf{x},h)$ is a spline based interpolation kernel with the kernel support of $2h$. It is a C^2-continuous function that approximates the shape of a Gaussian function with compact support. This allows smoothed approximation to any physical properties of the simulated material from the particle information. For example, the density can be estimated everywhere by

$$\rho(\mathbf{x}) = \sum_j m_j W(\mathbf{x}-\mathbf{x}_j,h). \tag{2.22}$$

For the rest of this thesis, we will not distinguish between a summation interpolant and the actual function since this will be clear from the context.

The smoothing formalism in (2.21) also provides a way to find gradients of properties. The gradient of the given function A is given by:

$$\nabla A(\mathbf{x}) = \sum_j m_j \frac{A_j}{\rho_j} \nabla W(\mathbf{x} - \mathbf{x}_j, h). \tag{2.23}$$

In SPH, the derivative is found by a derivative of the kernel function. Other linear operators can be treated similarly: the Laplacian ΔA can be approximated as

$$\Delta A(\mathbf{x}) = \sum_j m_j \frac{A_j}{\rho_j} \Delta W(\mathbf{x} - \mathbf{x}_j, h), \tag{2.24}$$

and the divergence of a vector-valued function A becomes

$$\nabla \cdot A(\mathbf{x}) = \sum_j m_j \frac{A_j}{\rho_j} \cdot \nabla W(\mathbf{x} - \mathbf{x}_j, h) \tag{2.25}$$

It can be seen that particle approximation in (2.21) and (2.23) converts the continuous integral representation of a function and its derivatives to the discretized summations based on an arbitrarily set of particles. This is a key approximation that makes SPH method simple without using a mesh for numerical integration.

2.2.2 Kernels

In the SPH method, the interpolation of any quantity at any point in space is based on kernel estimation. The interpolant in (2.18) reproduces A

exactly if the kernel is a delta function. In practice, the kernel are functions which tend to the delta function as the length scale h tends to zero as stated in (2.20). They are normalized to 1 so that the constants are interpolated exactly [47]. The original SPH proposed by Gingold and Monaghan [44] used a Gaussian kernel. In one dimension

$$W(\mathbf{x},h) = \frac{1}{h\sqrt{\pi}} e^{-(x^2/h^2)}, \tag{2.26}$$

which is the usual example of a sequence which mimics a delta function in the limit $h \to 0$. The Gaussian kernel is sufficiently smooth even for high orders of derivatives and it is very stable and accurate especially for disordered particles. However, since it is not compact and never goes to zero theoretically, Monaghan and Lattanzio devised a new smoothing function based on the cubic spline function known as B-spline function [49]

$$W(\mathbf{x},h) = \frac{\sigma}{h^{\nu}} \begin{cases} 1 - \frac{3}{2}q^2 + \frac{3}{4}q^3 & \text{if } 0 \le \frac{r}{h} \le 1; \\ \frac{1}{4}(2-q)^3 & \text{if } 1 \le \frac{r}{h} \le 2; \\ 0 & \text{otherwise} \end{cases} \tag{2.27}$$

where ν is the number of dimensions, r is distance, and σ is a normalization constant with the values $2/3$, $10/7\pi$, and $1/\pi$ in one, two, and three dimensions, respectively. Since the cubic spline kernel function resembles a Gaussian function while having compact support, that is, interactions are exactly zero for $r > 2h$, it has been the most commonly used smoothing function in the literature. Later, higher order spline kernel functions were also introduced to approximate the Gaussian more closely and more stably [50, 51]. However, since high order function is negative in some regions of its support domain, this may lead to unphysical results in some cases. In general cases, the cubic spline kernel function works well enough, however, sometimes a new kernel function needs to be devised to handle application specific issues. For the procedures and conditions for constructing smoothing functions, please refer to [46] for details.

2.2.3 Applications

Because SPH is essentially a technique for approximating the continuum equations, it can be used for a wide range of applications. It was originally developed by Gingold and Monaghan [44] for astrophysical applications and was extended to the simulation of incompressible fluid flows interacting with boundaries by Monaghan [52, 53]. SPH is well adapted for modeling coupled fluid flows, solid structure deformation and heat transfer. The particles represent volumes of discretized fluid or solids that move around in response to the fluid or solid stresses produced by interaction with other particles. The Lagrangian nature of SPH lets the particles automatically follow complex flows with all the computational information. This thesis is not related to fluid simulation, however, we will shortly explain how SPH is used for fluid simulation for better understanding of SPH. SPH framework for simulating deformable body will be presented in the next chapter.

The SPH representation of the hydrodynamic governing equations can be built from the Navier-Stokes equations.

Continuity equation

From [52] and [53] our preferred form of SPH continuity equation is:

$$\frac{\mathrm{d}\rho_a}{\mathrm{d}t} = \sum_b m_b \left(\mathbf{v}_a - \mathbf{v}_b\right) \nabla W_{ab} \tag{2.28}$$

where ρ_a is the density of particle a with velocity $\mathbf{v}_a$ and m_b is the mass of particle b. We denote the position vector from particle b to particle a by $\mathbf{r}_{ab} = \mathbf{r}_a - \mathbf{r}_b$ and let $W_{ab} = W(\mathbf{r}_{ab}, h)$ be the interpolation kernel with smoothing length h evaluated for the distance $|\mathbf{r}_{ab}|$.

This form of the continuity equation is Galilean invariant (since the positions and velocities appear only as differences), has good numerical conservation properties and is not affected by free surfaces or density discontinuities. The use of this form of the continuity equation is very important for predicting free surface flows such as those occurring in various forms of die casting and resin transfer molding.

As two particles approach each other, their relative velocity is negative (as is the gradient of the kernel) so that there is a positive contribution to $\frac{d\rho_a}{dt}$. If this rate of change is positive then the density of particle a rises leading to a positive pressure that pushes the particles apart again. If two particles move apart then their densities decrease creating a negative pressure that pulls the particles back towards each other. This interplay of velocity and density/pressure ensures that the particle remain 'on average' equally spaced and that the density is close to uniform so that the fluid is close to incompressible.

Momentum equation

The SPH momentum equation used is from [54]:

$$\frac{d\mathbf{v}_a}{dt} = -\sum_b m_b \left[\left(\frac{P_b}{\rho_b^2} + \frac{P_a}{\rho_a^2} \right) - \frac{\xi}{\rho_a \rho_b} \frac{4\mu_a \mu_b}{(\mu_a + \mu_b)} \frac{\mathbf{v}_{ab} . \mathbf{r}_{ab}}{\mathbf{r}_{ab}^2 + \eta^2} \right] \nabla_a W_{ab} + \mathbf{g} \,, \tag{2.29}$$

where P_a and μ_a are pressure and viscosity of particle a and $\mathbf{v}_{ab} = \mathbf{v}_a - \mathbf{v}_b$. Here η is a small parameter used to smooth out the singularity at $\mathbf{r}_{ab} = 0$ and $\mathbf{g}$ is the gravity vector.

The first two terms involving the pressure correspond to the pressure gradient term of the Navier-Stokes equation. The next term involving viscosities is the Newtonian viscous stress term. This form ensures that stress is automatically continuous across material interfaces and allows the viscosity to be variable or discontinuous.

The time step for the explicit integration used in these simulations is limited by the Courant condition modified for the presence of viscosity:

$$\Delta t = \min_a \left\{ 0.5h / (c_s + \frac{2\xi\mu_a}{h\rho_a}) \right\}. \tag{2.30}$$

where c_s is the local speed of sound.

Equation of State

This version of SPH is a compressible method which is used near the incompressible limit by using a sound speed that is much larger than the velocity scales in the flow. This quasi-incompressible limit is actually what happens with real fluids. The equation of state, giving relationship between particle density and fluid pressure, is:

$$P = P_0 \left[\left(\frac{\rho}{\rho_0}\right)^{\gamma} - 1 \right] \tag{2.31}$$

where P_0 is the magnitude of the pressure and ρ_0 is the reference density. For water the exponent $\gamma = 7$ is used. This pressure is then used in the SPH momentum equation (2.29) to give the the particle motion.

The pressure scale factor P_0 is given by:

$$\frac{\gamma P_0}{\rho_0} = 100V^2 = c_s^2 \,. \tag{2.32}$$

where V is the characteristic or maximum fluid velocity. This ensures that the density variation is less than 1% and the flow can be regarded as incompressible. For complex flow with wide jets even lower levels of compressibility are required.

The simulation progresses by explicitly integrating this system of ordinary differential equations in (2.28) and (2.29). The form of these equations are the same regardless of the dimensionality of the governing equations. There is no reference to any computational grid. The particle position is the only geometric term in the equations. The computation of the sums in the equations requires only the identification of the particles' neighboring particles.

In summary, the SPH method requires no computational grid. The SPH particles carry all the computational information and they are free to move. The Lagrangian nature of SPH means that the particles will automatically follow complex flows. This makes the method particularly suited for fluid flows involving complex free surface motion. It is relatively easy to apply the method to multi-dimensional problems.

Chapter 3

Volume-Preserving Deformation of Particles

3.1 SPH for Deformable Objects

While SPH is most widely used for fluid dynamics these days, SPH is also used to simulate deformable objects based on linear elasticity [55, 56, 57, 58]. In linear elasticity, the strain ε and the stress σ are modeled by a linear relationship $\sigma = \mathbf{C}\varepsilon$, which is known as Hooke's law. For isotropic materials, $\mathbf{C}$ depends only on the Young's modulus E and the Poisson's ratio ν. In matrix form, Hooke's law for isotropic materials can be written as

$$\begin{bmatrix} \sigma_{xx} \\ \sigma_{yy} \\ \sigma_{zz} \\ \sigma_{xy} \\ \sigma_{yz} \\ \sigma_{xz} \end{bmatrix} = \frac{E}{(1+\nu)(1-2\nu)} \begin{bmatrix} 1-\nu & \nu & \nu & 0 & 0 & 0 \\ \nu & 1-\nu & \nu & 0 & 0 & 0 \\ \nu & \nu & 1-\nu & 0 & 0 & 0 \\ 0 & 0 & 0 & 1-2\nu & 0 & 0 \\ 0 & 0 & 0 & 0 & 1-2\nu & 0 \\ 0 & 0 & 0 & 0 & 0 & 1-2\nu \end{bmatrix} \begin{bmatrix} \varepsilon_{xx} \\ \varepsilon_{yy} \\ \varepsilon_{zz} \\ \varepsilon_{xy} \\ \varepsilon_{yz} \\ \varepsilon_{xz} \end{bmatrix} . \tag{3.1}$$

To define elastic forces between particles, the strain energy U_i of a particle *i* needs to determine as follows:

$$U_i = \bar{v}_i \frac{1}{2}(\varepsilon_i \cdot \sigma_i), \tag{3.2}$$

where $\bar{v}_i$ is the volume of particle *i*. The elastic force $F^{elastic}$ can be defined as the negative gradient of strain energy U with respect to displacement $\mathbf{u}_i$ of a particle *i*, which corresponds to the difference between its original position $\mathbf{x}_i^0$ and current position $\mathbf{x}_i$. By employing Green-Saint-Venant strain tensor [56, 57], the internal elastic force from particle *i* to particle *j* is given by:

$$F_{ji}^{elastic} = -\nabla_{\mathbf{u}_j} U_i = -2\bar{v}_i(\mathbf{I} + \nabla\mathbf{u}_i^T)\sigma_i \mathbf{d}_{ij}, \tag{3.3}$$

where $\mathbf{I}$ is the identity matrix, $\nabla\mathbf{u}_i$ is the gradient of the displacement from the reference configuration, and $\mathbf{d}_{ij}$ is defined by

$$\mathbf{d}_{ij} = \frac{\partial \nabla\mathbf{u}_i}{\partial \mathbf{u}_j}. \tag{3.4}$$

In SPH formulation, $\nabla\mathbf{u}$ and $\mathbf{d}_{ij}$ are defined as

$$\nabla\mathbf{u}_i = \sum_j \bar{v}_j \mathbf{u}_{ji} \nabla W(\mathbf{x}_{ij}^0, h)^T, \tag{3.5}$$

$$j \neq i \rightarrow \mathbf{d}_{ij} = \bar{v}_j \nabla W(\mathbf{x}_{ij}^0, h), \tag{3.6}$$

$$\mathbf{u}_{ji} = \mathbf{u}_j - \mathbf{u}_i = \mathbf{x}_j - \mathbf{x}_i - (\mathbf{x}_j^0 - \mathbf{x}_i^0). \tag{3.7}$$

As the deformation gradient employed in the above has only zero order consistency, rotations of particles introduce strain and corresponding elastic forces, which prevent the objects from rotating. To resolve this rotation problem, the corotated SPH has been proposed that decomposes a deformation gradient $\nabla\mathbf{u}$ into a rotational part and a stretching part based on the shape matching procedure [58, 59]. In the shape matching procedure, the rotation for each object is extracted from the transformation matrix

$$\mathbf{M} = (\sum_i m_i \mathbf{p}_i \mathbf{q}_i^T)(\sum_i m_i \mathbf{q}_i \mathbf{q}_i^T)^{-1} := \mathbf{M}_{pq}\mathbf{M}_{qq}, \tag{3.8}$$

where $\mathbf{q}_i = \mathbf{x}_i^0 - \mathbf{x}_{cm}^0$ and $\mathbf{p}_i = \mathbf{x}_i - \mathbf{x}_{cm}$ are relative particle positions with respect to the center of mass(cm) of a body in the initial and current states, respectively. Since $\mathbf{M}_{qq}$ is symmetric, the rotation matrix can be obtained from $\mathbf{M}_{pq}$ using a polar decomposition. To compute an individual rotation matrix for each particle instead of a rotation matrix for an object, Becker *et al.* [58] proposed an SPH formulation for the matrix $\mathbf{M}_{pq}$ for a particle i as follows:

$$\mathbf{M}_{pq_i} = \sum_j m_j W(\mathbf{x}_{ij}^0, h)\left((\mathbf{x}_j - \mathbf{x}_i)(\mathbf{x}_j^0 - \mathbf{x}_i^0)^T\right). \tag{3.9}$$

Now the rotation matrix $\mathbf{R}_i$ for a particle i can be computed as follows:

$$\mathbf{R}_i = \mathbf{M}_{pq_i}\mathbf{S}_i^{-1} \tag{3.10}$$

where $\mathbf{S}_i^{-1}$ is computed through a polar decomposition. Once the rotation matrix for each particle is obtained, the deformation gradient in (3.5) can be computed as follows:

$$\nabla\mathbf{u}_i = \sum_j \bar{v}_j \tilde{\mathbf{u}}_{ji} \nabla W(\mathbf{x}_{ij}^0, h)^T, \tag{3.11}$$

where $\tilde{\mathbf{u}}_{ji}$ is the locally rotated deformation given by

$$\tilde{\mathbf{u}}_{ji} = \mathbf{R}_i^{-1}(\mathbf{x}_j - \mathbf{x}_i) - (\mathbf{x}_j^0 - \mathbf{x}_i^0). \tag{3.12}$$

Finally, the elastic force $\mathbf{f}_i$ at each particle is computed in a symmetrized way as

$$\mathbf{f}_i = \sum_j \frac{-\mathbf{R}_i \bar{f}_{ji} + \mathbf{R}_j \bar{f}_{ij}}{2}. \tag{3.13}$$

$\bar{f}_{ji}$ and $\bar{f}_{ij}$ are the forces derived from (3.3) using the modified deformation gradient in (3.11).

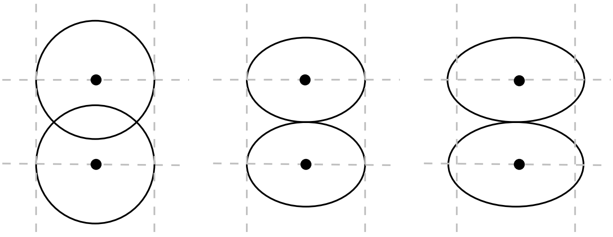
(a) (b) (c)

Figure 5: Deformed particles. (a) Overlapped particles in the corotated SPH method. (b) Particles rearranged with a minimized overlap but with volume loss. (c) Particles after the application of our volume preserving scale matrix.

3.2 Volume-Preserving Deformable Particle

The SPH for deformable objects described above computes the elastic force between particles from the strain energy based on the change of relative positions of the particles. In the original SPH, the particles of an object are overlapped and departed by the external force, resulting in the change of the object volume. Even though the change of volume is natural for the linear elasticity, it sometimes needs to be minimized to preserve the volume of the simulated object or a part of it. For example, the volume of metastasis in the liver should be preserved during the registration. To support such a volume-preserving registration, we propose a novel method which conserves the volume of each particle in the volume-preserving region (i.e., candidate region of metastasis) during the deformation of particles.

In the corotated SPH, $\mathbf{M}_{pq_i}$ in (3.9) can be decomposed into a rotation and scaling matrices. In the decomposition, Singular Value Decomposition(SVD) can be used instead of the polar decomposition [60]. The decomposed scaling matrix contains the local volume change information of a particle (e.g. compression or expansion). By applying the scaling matrix to each particle, we can obtain rearranged particles to minimize the overlaps between particles [see Fig. 5(b)]. In order to make each particle preserve its original volume, we modify the scaling factor so that the multiplication of scaling factor in each axis is equal to unity. Using this proposed method, the original volume of each particle is well preserved along with a minimized overlap between particles [see Fig. 5(c)]. In our method, (3.11) and (3.12) are updated to include the scaling matrix for the calculation of the internal elastic force as follows:

$$\nabla \mathbf{u}_i = \sum_j \bar{v}_j \hat{\mathbf{u}}_{ji} \nabla W(\mathbf{x}^0_{ij}, h)^T, \tag{3.14}$$

where

$$\hat{\mathbf{u}}_{ji} = \mathbf{S}_i^{-1} \mathbf{R}_i^{-1} (\mathbf{x}_j - \mathbf{x}_i) - (\mathbf{x}^0_j - \mathbf{x}^0_i). \tag{3.15}$$

Since $\hat{\mathbf{u}}_{ji}$ in (3.15) inappropriately cancels out the restoration force which originally exists before scaling, $\hat{\mathbf{u}}_{ji}$ is modified as follows:

$$\begin{aligned}\hat{\mathbf{u}}_{ji} &= \mathbf{S}_i^{-1}\mathbf{R}_i^{-1}(\mathbf{x}_j-\mathbf{x}_i)-(\mathbf{x}_j^0-\mathbf{x}_i^0) \\ &\quad -\frac{\mathbf{S}_i^{-1}(\mathbf{x}_j^0-\mathbf{x}_i^0)-(\mathbf{x}_j^0-\mathbf{x}_i^0)}{2}.\end{aligned} \tag{3.16}$$

Fig. 6 compares the proposed method with the previous corotated SPH method by showing the shape change of particles when the external force is exerted on a box-shaped object. The deformable body is dropped to the static floor using gravity. In the corotated SPH method, the particles are overlapped, resulting in the overall volume loss [see Fig. 6(a)]. In contrast, our method preserves the volume of each particle by compressing it in the overlapping direction and expanding it to direction perpendicular to the overlapping direction, keeping the multiplication of three scaling factors in x-, y-, and z-axes constant [see Fig. 6(b)].

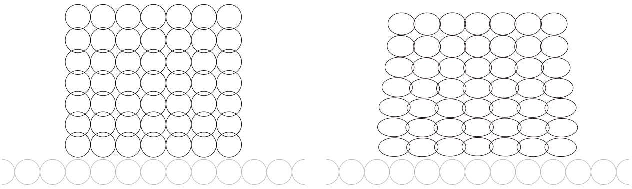

(a) (b)

Figure 6: Deformation of an object after being dropped to the floor. (a) Particles in the corotated SPH method are overlapped, suffering from the overall volume loss. (b) Particles in the proposed method are deformed while minimizing the overlap and preserving the volume of each particle. The particles in the lower position are deformed more. Grey particles represent a static floor object.

Chapter 4

Non-Rigid Registration with the Deformable Particles

The physically based registration methods are largely classified into two groups according to the materials to model the objects. The first group models the object as fluid material and applies fluid dynamics to the deformation [28, 42, 39], and the other group models the object as elastic material to simulate the shape change [38, 26, 43, 27]. The fluid-model methods, in which the forces for moving fluid are computed from the change in the viscosity and pressure of the fluid, can freely deform the object regardless of its initial shape, enabling large deformation. On the other hand, the elastic-model methods, which compute the forces from strain energy, preserve the initial shape of the object relatively well, and thus they are more suitable for simulating local deformation. In our method, we model the liver as elastic material because the liver should be deformed while keeping its overall shape and local connectivity.

The physically based registration methods also can be classified into Eulerian and Lagrangian methods regarding how to represent a simulation space in the deformation. Eulerian methods divide the simulation space into grids and simulate the change of material at the grid points whereas Lagrangian methods divide the material itself into small elements (i.e., particles) and trace those elements during the simulation. We adopt a Lagrangian method because particles are more suitable for representing a moving object with spatially varying physical properties (e.g. varying stiffness in the liver).

The goal of image registration is to find an optimal transformation $\mathbf{T} : \Omega_{Float} \to \Omega_{Ref}$ such that the source floating image (i.e. follow-up scan), $I_{Float} : \Omega_{Float} \subset \mathbf{R}^d \to \mathbf{R}$, best matches the target reference image (i.e. original scan), $I_{Ref} : \Omega_{Ref} \subset \mathbf{R}^d \to \mathbf{R}$. As the liver exhibits a relatively large difference between the source and target images due to the movement and breathing, our liver registration method consists of the global registration with rigid transformation and the local registration with the physically based registration method.

Our registration method is composed of the following steps as shown in Fig. 7. As a preparation stage, we automatically detect the liver and the volume-preserving region around the metastasis. Particles are placed in the detected regions (i.e., the liver and candidate regions of metastasis) in the source image, and a GVF-based force field is generated in the target image. Subsequently, we perform rigid registration for global image matching, which serves as an initial estimate for the next non-rigid registration. We

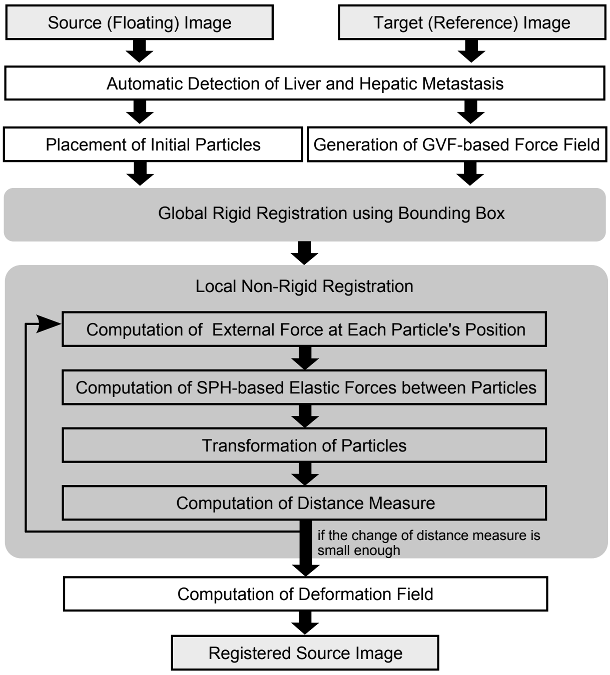

Figure 7: Process of particle-based volume preserving follow-up liver CT registration

then perform non-rigid registration for local matching using the proposed physically based registration method.

4.1 Automatic Detection of Liver and Candidate Regions of Metastasis

The liver is difficult to automatically segment due to its high variation in shape and the similar intensity of nearby organs including the heart, pancreas, spleen, and kidneys [61]. In this paper, we apply an automatic liver segmentation method based on a level-set algorithm [61]. This method utilizes level-set speed images for more optimal estimation of an initial liver shape, achieving faster and more robust segmentation of liver.

The metastasis is also elusive to automatically segment due to its ambiguous boundary and large variability in the shape, size, and location in the liver [62]. Thus, instead of segmenting the exact region of metastasis, we automatically detect candidate regions of metastasis in the source image. Based on the fact that metastases are relatively darker than other regions of the liver parenchyma in portal-phase CT image [10], the image intensity is considered to detect candidate regions of metastasis. The voxel is determined to be in the candidate regions of metastasis if the intensity is lower than a user-defined threshold, $T_{intensity}$, which was empirically set to be 100 HU. However, only with the intensity value, other regions in the liver that are not metastases can be inappropriately detected [see Fig. 8(b)]. To remove these false positives, the sphericity is additionally considered based on the fact that metastases have nearly spherical or ellipsoid shapes [63]. Each candidate region of metastasis detected by the intensity criterion is identified as an object by applying connected component analysis [64]. Then, the sphericity of each object is defined as the ratio of the surface area of a sphere (having the same volume as the given object) to the surface area

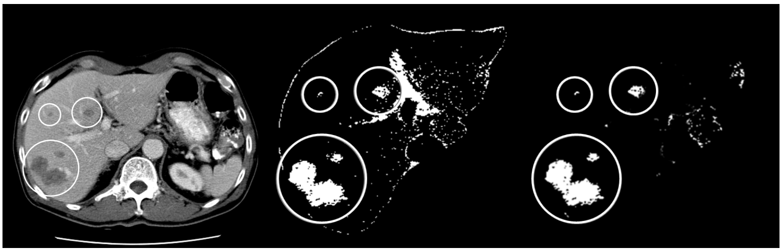

(a) (b) (c)

Figure 8: Candidate regions of metastases. The metastasis is enclosed by the solid circle. (a) is the floating image. White regions in (b) are the regions detected by considering only the intensity. White regions in (c) are the candidate regions of metastases by considering both the intensity and sphericity.

of the object:

$$\Psi = \frac{\pi^{\frac{1}{3}}(6V_o)^{\frac{2}{3}}}{A_o}, \tag{4.1}$$

where V_o is the volume of the object and A_o is the surface area of the object. The object is determined to be the candidate region of metastasis if the sphericity is higher than a user-defined threshold, $T_{sphericity}$, which was set to be 0.3. The small object with the size less than 10 voxels can be regarded as noise and is discarded. By using both intensity and sphericity, candidate regions of metastases are more accurately found, as shown in Fig. 8(c). In the following non-rigid registration, the detected candidate regions of metastasis are modeled with volume-preserving particles so that the growth of metastasis can be accurately assessed (described in detail later).

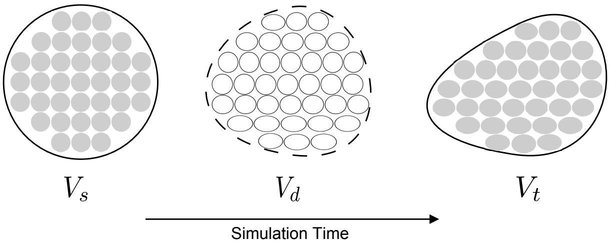

Figure 9: Deformation process. Particles filling the source shape $\mathbf{V}_s$ are deformed to a deformed shape $\mathbf{V}_d$, finally fitting into the target shape $\mathbf{V}_t$.

4.2 Placement of Initial Particles in Source Image

For ease of explanation, the segmented regions in the source and target images are called as the source shape $\mathbf{V}_s$ and a target shape $\mathbf{V}_t$, respectively. Particles are initially generated and placed in the source shape which we want to deform to finally fit into the target shape as shown in Fig. 9. A particle is the minimal element of the deformation simulation and its size determines the resolution of a simulation. For better simulation quality, the object under simulation needs to be modeled with smaller particles and with an accordingly increased number of particles. However, the computation time is directly proportional to the number of particles so that the size of particles needs to be determined considering a trade-off between simulation quality and performance.

In medical datasets, a single object (e.g. organ) can have a complex

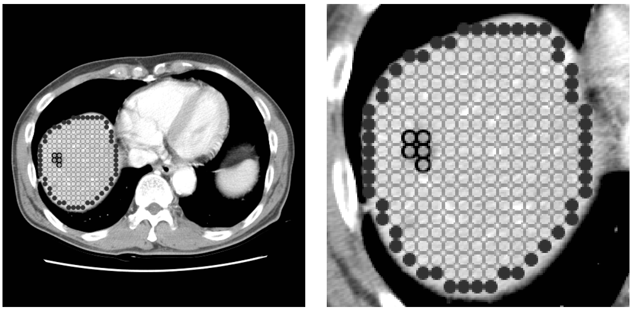

Figure 10: Particles initially placed in the source shape of liver (left) and in its magnified view (right). The particles of a fixed size are regularly placed in the liver. Light-grey-lined, black-lined, and black-filled particles represent normal liver particles, metastasis particles, and boundary particles, respectively.

physical property which varies spatially. For example, tumors in an organ are stiffer than the normal tissue of that organ [5, 6, 7]. A particle in our method can carry its own mechanical properties during the simulation. If some part of V_s needs to have different properties, different property values can be assigned to the particles. In our method, the metastasis is filled with particles with higher stiffness property (e.g. higher Young's modulus) by exploiting the fact that the metastases are stiffer than other normal cells in the liver parenchyma. The corresponding physical properties stored in the particle are used when the elastic force is calculated between particles.

During the particles placement, the particles near the boundary of the segmented liver are defined as boundary particles. In our method, these boundary particles will mainly lead the deformation process during the simulation (explained in detail later). Fig. 10 shows the particles filling the source shape of liver in a 2D abdomen CT image.

4.3 Generation of GVF-based Force Field in Target Image

After the particles are placed in the source shape, we generate an external force field from $\mathbf{V}_t$ in the target image by using a GVF method [65], which moves the particles initially staying inside $\mathbf{V}_s$ to inside $\mathbf{V}_t$. The external GVF force field directed to the boundary of the target shape leads the boundary particles in the source shape to the target boundary. The GVF forces, which are derived from a diffusion operation, tend to extend far away from the target shape. The diffusion process also creates forces which can pull the particles even into a concave region. Such far-extending force range of the GVF force field and its ability to handle concave region make it useful for moving the boundary particles in the source shape to the arbitrary target shape which might be very far away from the source shape.

GVF field is the vector field $\mathbf{v}(x,y,z) = (u(x,y,z), v(x,y,z), w(x,y,z))$ that minimizes the following energy functional:

$$\begin{aligned} \varepsilon &= \int\int\int \mu(u_x^2 + u_y^2 + u_z^2 + v_x^2 + v_y^2 + v_z^2 \\ &\quad + w_x^2 + w_y^2 + w_z^2) + |\nabla f|^2 \, |\mathbf{v} - \nabla f|^2 \, dxdydz, \end{aligned} \tag{4.2}$$

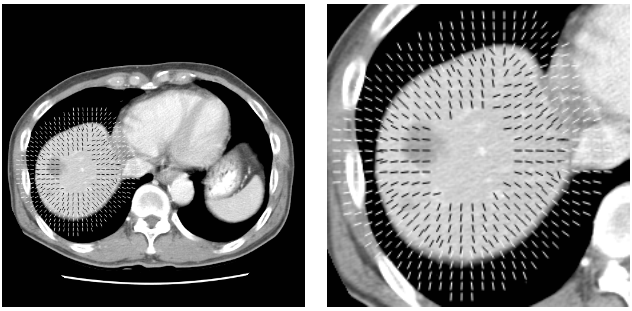

Figure 11: GVF-based force field from the target shape of liver. The forces in black are external forces acting outward from inside to the target boundary. The forces in white are external forces acting inward from outside to the target boundary.

where μ is a regularization parameter determining the relative weight between the first and second terms. If $|\nabla f|$ is small, the energy is dominated by the first term consisting of the partial derivatives of the vector field, yielding a smooth vector field. If $|\nabla f|$ is large, the energy is dominated by the second term, which makes the vector field $\mathbf{v}$ be equal to ∇f. In this case, the resulting GVF force field near the object boundary points toward the boundary while it varies smoothly over homogeneous regions. In other words, the magnitude of the resulting GVF vectors gets bigger as it approaches to the boundary, making particles accelerated more at the boundary. Since it is not required in our case, we normalize the force field and only keep the directions. The normalized GVF force field can be also easily scaled up to globally control the acceleration of particles appropriately. Fig. 11 shows the normalized GVF force field for a 2D case.

As the particles forming an object are strongly connected to each other, a moving particle affects its neighboring particles. If the external force field, which covers whole simulation space, affects all the particles, the inside particles might falsely cause the boundary particles to go over the target boundary, resulting in inaccurate registration. Instead, our method makes the external force field affect only the boundary particles while letting the other inside particles follow the boundary particles indirectly through interactions between particles.

The proposed registration method deforms an object by using the boundary information, but it does not find one-to-one correspondences between the boundary particles of $\mathbf{V}_s$ and $\mathbf{V}_t$. One-to-one correspondence between the boundaries of $\mathbf{V}_s$ and $\mathbf{V}_t$ can provide an exact solution to the simulation [43]. However, finding such correspondence is almost impossible for the liver because the liver does not have any specific features which can be used as anatomical landmarks (e.g. sulcal fundi in brain, taeniae coli in colon, and hilar points in lung). And thus, we attempt to find a solution by deforming the liver through physical interactions between particles for a given change of the boundary shape and by finding a balanced status of particles.

4.4 Non-Rigid Registration with Particles

After the initial particles are placed in the source shape and the external force field is generated from the target boundary, the particles are ready to move through a simulation for non-rigid registration between the source and target images. Prior to the non-rigid registration, we globally register the source and target shapes using their bounding volume information. The bounding volumes of $\mathbf{V}_s$ and $\mathbf{V}_t$ are computed, and the initial particles in the source shape are translated so that the center of the bounding volume of $\mathbf{V}_s$ is located at the center of that of $\mathbf{V}_t$.

After the global rigid registration, the boundary particles in the source shape start to move following the external force field, changing the shape of the object in the source image. The internal particles then begin to move through interactions between particles governed the linear elasticity using SPH. The methods to simulate a deformable object using SPH and a novel deformable particle approach described in Chapter 3 are applied at this stage for the registration.

While the external force field moves the boundary particles of $\mathbf{V}_s$ into the boundary of $\mathbf{V}_t$, the distance measure determines the convergence of the simulation to stop the simulation. The distance measure is calculated using the geometric information of how much the deformed shape of the source shape $\mathbf{V}_s$, called as $\mathbf{V}_d$, differs from the target shape $\mathbf{V}_t$. To calculate the distance measure, a 3D distance map is generated from the target shape $\mathbf{V}_t$ using the chamfer distance transform [66], in which each voxel in the distance map stores the chamfer distance to the nearest voxel in the target boundary. The distance measure is computed by averaging the distance values of the boundary particles in the distance map as follows:

$$\mathbf{ADE} = \frac{1}{N_{bp}} \sum_{i=0}^{N_{bp}-1} DistanceMap(Transform(P_i)) \tag{4.3}$$

where **ADE** represents the average distance error between boundary particles and boundaries of $\mathbf{V}_t$, N_{bp} is the number of boundary particles, P_i is a boundary particle of $\mathbf{V}_s$, $Transform(P_i)$ is the transformed position of each boundary particle, P_i, and $DistanceMap(Transform(P_i))$ represents the shortest distance between a transformed boundary particle and boundary surface of $\mathbf{V}_t$. We measure the **ADE** after each simulation iteration. If the **ADE** difference between the previous and current iterations is less than a specified threshold (indicating that the movement of the particles is mostly stabilized), the simulation terminates. Please note that the particles move relatively slow at the beginning of the simulation until they become accelerated to a sufficient extent. Thus, we apply the termination criteria after a specific number of simulation iterations in order to distinguish the small movement of the particles at the beginning from that of the stabilized particles.

4.5 Computation of Deformation Field

After the simulation is finished, we compute the deformation field for voxels in the source image using the deformed particles. For a voxel with the position $\mathbf{x}_i$, we identify the deformed particles within a specific distance l as shown in Figure 12. For l, we used $r \times \sqrt{dim}$, where r is the particle's radius and dim is the dimension. If one or more particles are identified, we calculate the deformation vector of each particle using its initial and deformed position. The deformation vector $\mathbf{r}$ of the voxel of the position $\mathbf{x}_i$ is interpolated through the SPH approximation in (2.21) as follows:

$$\mathbf{r}(\mathbf{x}_i) = \sum_j m_j \frac{\mathbf{x}_j^0 - \mathbf{x}_j}{\rho_j} W(\mathbf{x}_i - \mathbf{x}_j, h), \tag{4.4}$$

where $\mathbf{x}_j^0$ is the initial position of the particle j. If no particle is identified nearby, it indicates that this voxel is outside the deformed object, thus the voxel has a zero deformation vector. A deformed volume in 3D is finally acquired by calculating the deformation vectors at every voxels. In general, image registration methods obtain deformation field for the source or floating image and deforms the source image by moving the pixels in the image using the displacement vectors. However, there could be holes in the de-

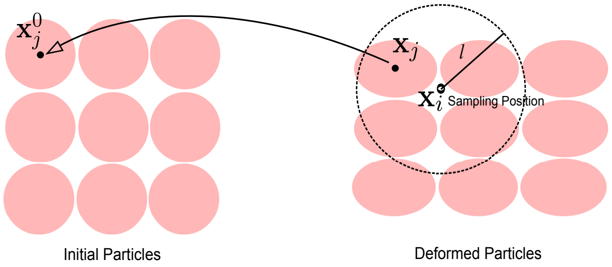

Figure 12: Sampling deformation field for image deformation. The deformation field is computed by interpolating neighbor particle's displacement at the sampling positions.

formed image in this case. In our case, we find displacement vectors for the pixels in the deformed image by interpolating displacements of particles in the final positions and obtain pixel intensity values from the source image using these vectors. This reversed sampling makes the final deformed image smooth without any holes in it.

Chapter 5

Implementation

In the previous chapters, conceptual workflow and mathematical details on each step of the SPH based non-rigid registration method was given. The issues on implementing the proposed method will be described in this chapter. The main algorithm was implemented using standard C++ and GUI was developed using Qt library for multi-platform support. For the visualization of particles in 3D, OpenGL library was used. In the following sections, the flow of main algorithm will be described first and issues on managing particles in the scene and computing timesteps for the simulation will be followed.

5.1 Workflow

Given two sets of source and target images, the preprocessing stage begins by detecting liver and candidate regions of metastasis in the images. The regions can be automatically detected using the algorithm in Section 4.1 or manually segmented by the abdomen radiologists. Since the images scanned using medical imaging scanners have unequal scanning resolution in different dimensions, i.e., difference between section thickness and pixel size, the segmented images are now converted into regular volume data using the method in [67]. The liver region in the source volume data is the source shape, $\mathbf{V}_s$, and that in the target volume data is the target shape, $\mathbf{V}_t$, in Chapter 4. Now, the source shape is filled with initial particles of user-defined size. The particles are placed with spacing of particle size by traversing voxels and checking if the current voxel is inside the source shape or not. User-defined mechanical properties are assigned to the particles according to their type, i.e., normal liver or metastasis. These types were already defined at the segmentation stage. Optionally, data structures for managing particles and for speed-up finding neighboring particles can be used. If it is used, it needs to be initialized at this stage. Then, force field to initiate and guide the registration process is generated from the target shape using GVF method [65]. The vectors in the force field will be used to direct particles to the boundary of the target shape. Next, a distance map for measuring similarity between a deformed source shape and the target shape is generated from the target shape using the chamfer distance transform [66]. This distance map will be used to check how far the particles at the boundary of deformed shape are placed from the target shape and the average of these distances is used as a similarity measure through the simulation. The preprocessing stage finishes by computing the timestep for simulation based on the mechanical properties used. This will be discussed in a following section.

Algorithm 1 Overall workflow

```
Input : source and target CT images, particle size and mechanical properties of material
Output : deformed source images
  Detect liver and candidate regions of metastasis
  Contstruct regular volume data from segmented input images
  Fill the detected regions in the source image with particles
  Initialize simulation domain
  Compute GVF force field from the liver region in the target image
  Compute distance map from the liver region in the target image
  Compute $timestep$
  $time \leftarrow 0$
  $diffADE, prevADE \leftarrow \infty$
  while $diffADE \geq threshold$ do
    Update domain information
    for each particle do
      Apply external force obtained from GVF force field
      Find neighbor particles
      for each neighbor particle do
        Compute interacting force between particles
      end for
    end for
    Update particle positions
    Compute corotation matrix rotation matrix
    Compute distance measure $ADE$
    $diffADE \leftarrow prevADE - ADE$
    $prevADE \leftarrow ADE$
    $time \leftarrow time + timestep$
  end while
  Compute the final deformed source image
```

If the preprocessing steps are finished, actual simulation begins. For each particle, external force at the particle's position is interpolated from the GVF force field and particle's acceleration is initialized with that force.

Then, particles which can influence the current particle are searched from the particle list and interacting forces between those particles and the current particle is computed one by one. The interacting elastic forces are accumulated and new velocity and position of the particle is determined after all interactions are handled. Once particles' new positions are determined, the similarity measure, i.e., ADE is computed and proceeds the simulation if the change of ADE is bigger than threshold. The overall algorithm is given in Algorithm 1.

5.2 Neighbor Search

When force is computed for a particle in the scene through the simulation, influences from all other particles in the simulation domain should be considered in theory and computing elastic forces between all the pairs of particles in the domain is a time consuming job. However, with the help of compact support property of smoothing kernel in SPH, only particles in limited range influence the particle at hand. Therefore, a data structure to manage particles in the scene is needed for fast look-up of candidate particles. In our implementation, we divided the simulation domain into regular cells and let each cell know which particles are in it as shown in Figure 13 (a). Given a particle's diameter d, h is $1.2 \times d$ and the width of cell is determined to $2h$ since our kernel's support is $2h$. The particle list in each cell

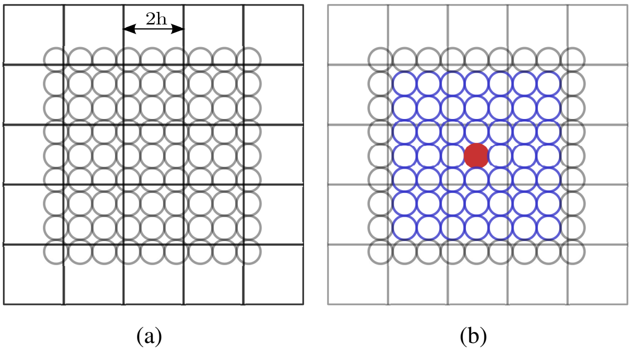

(a) (b)

Figure 13: Devision of simulation domain for fast neighbor search. (a) shows regular cells dividing simulation domain with particles in it and (b) shows candidate particles for the force computation. When force is computed for the particle colored in red, particles in neighboring cells are searched and force is computed only with those particles. The candidate particles are colored in blue.

is updated every time step by traversing particles in the scene and assigning them to a cell based on its current position. When interacting, i.e., elastic, force needs to be computed for a particle, the cell containing the particle is checked first and other particles in the cell and particles in the neighboring cells of the cell are registered as candidate particles as shown in Figure 13 (b). The red particle in Figure 13 (b) is the current particle that we are computing force and blue particles are the candidate particles found. The figure only shows small part of entire scene and there could be much more particles and cells in actual simulations. Even though some particles located relatively far from the current particle can be included to the candidate particle list, force computation with them can be terminated early by checking actual distance between two particles. Furthermore, if symmetric form of equation is used as described in [52], force can be computed only once for a pair of particles at a time step for further speed-up. Instead of the regular cells, $k-d$ trees can be used to manage the particles to efficiently compute these neighborhoods [68].

5.3 Time Integrator and Time Step

To move the particles to new positions at each time step, we used a predictor-corrector leap-frog integration which is computationally efficient as well as accurate [69]. The leap-frog integration got its name from the fact that the velocities leap over the positions, and vice versa. To integrate the set of equations describing the change of velocity $\mathbf{v}$ and position $\mathbf{x}$ given by

$$\frac{d\mathbf{v}}{dt} = \mathbf{f}, \tag{5.1}$$

and

$$\frac{d\mathbf{x}}{dt} = \mathbf{v}, \tag{5.2}$$

we denote the values of the variables at the beginning of a time step by $\mathbf{v}^0, \mathbf{f}^0, \mathbf{x}^0$, and the time step Δt. The predictor step is

$$\mathbf{v}_p = \mathbf{v}^0 + \Delta t \mathbf{f}^0, \tag{5.3}$$

and

$$\mathbf{x} = \mathbf{x}^0 + \Delta t \mathbf{v}^0 + \frac{1}{2}(\Delta t)^2 \mathbf{f}^0. \tag{5.4}$$

Then, new values of **f** are calculated using the predicted quantities, and the corrected values of **v** is calculated according to

$$\mathbf{v} = \mathbf{v}_p + \frac{1}{2}\Delta t(\mathbf{f} - \mathbf{f}^0). \tag{5.5}$$

Here, the value of position **x** is not corrected.

We chose the timestep smaller than the threshold $\Delta t = \frac{h}{v_{max}}$ to avoid self-penetration, where h stands for the minimum kernel dimension and v_{max} is the maximum particle velocity. The v_{max} is computed from the speed of sound in a material,

$$v_{max} = \sqrt{\frac{Young's\ modulus}{density}}. \tag{5.6}$$

As the timestep evaluation shows in Section 6.6, the processing time of particle based simulation method depends on the size of particles (i.e., the number of particles) and the maximum speed of the particles. A stiff material usually induces strong interacting force for the same amount of displacement compared to a less stiff material, resulting in faster movement of particles. To deal with those fast moving particles, a smaller time step is required for the simulation with stiffer particles, which also increases the simulation time.

5.4 Terminating Condition

The simulation stops if the internal force which is caused by the deformation of elastic material and the external force which acts on the elastic body from outside form an equilibrium solution. The change of similarity measure, i.e., the average distance error (*ADE*), is used to determine if the simulation is in equilibrium state in the proposed method. The simplest form of terminating condition is checking if the change of *ADE* between the previous and current iterations is less than pre-defined threshold as described in Algorithm 1. Since the particles move relatively slow at the beginning of the simulation until they become accelerated to a sufficient extent, we apply the termination criteria after a specific number of simulation iterations in order to distinguish the small movement of the particles at the beginning from that of the stabilized particles.

In some cases, instant overlap between particles which is caused by scaling of particles can produce strong force between particles resulting in instant increase of *ADE* even though equilibrium state is not reached yet. Therefore, a terminating condition which can deal with this error case needs to be devised. In our implementation, we stored history of *ADE* during simulation and let the simulation terminate only when the averaged ADE of recent m time steps exceeds the averaged ADE of recent $n\,(n > m)$ time steps. This made the terminating condition less sensitive to the erratic case than the simple one, however, this also can make the simulation run longer than needed because it does not stop right after reaching the equilibrium state.

Chapter 6

Results

Registration was performed on follow-up abdominal CT scans of 10 patients who had metastases. The number of slices per scan ranged from 30 to 44. Each image had a matrix size of 512 × 512. A section thickness was 5.0 mm, and pixel sizes ranged from 0.617 to 0.676 mm. All datasets had noticeable changes (more than 97 %) in metastasis volume. The average number of metastases per scan was 2.7 (range, 1-5). We compared the proposed method ($\mathbf{NR}_{Proposed}$) with two other methods: the corotated SPH method ($\mathbf{NR}_{SPH}$) and conventional method using B-spline ($\mathbf{NR}_{B-spline}$) [1, 2].

6.1 Phantom Study

We conducted two phantom studies. First, we performed the simulation in which the interacting particles have different physical properties [see Fig. 14]. In this study, particles in right side of the object have higher Young's modulus (i.e., high stiffness). As shown in Fig. 14(b), when the object is dropped to the floor, the left side of the object collapses to a greater extent than does the right side. This property can be used to effectively model the

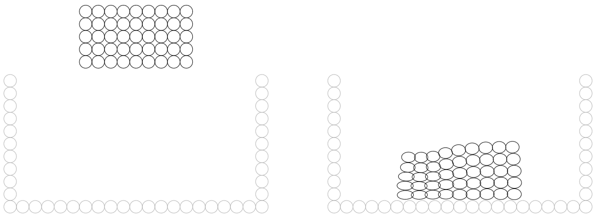
(a) (b)

Figure 14: Simulation of a box object composed of materials with various Young's modulus. (a) Initial status in which the particles in left and right sides of the box have lower and higher Young's modulus, respectively. (b) Simulated result when the box is dropped to the floor.

behavior of metastases during the liver registration (presented in the next sections). As mentioned earlier, the metastasis is known to be stiffer than other normal cells in the liver parenchyma [5, 6, 7].

In the second phantom study, we applied the proposed method to the registration of 2D images. In this study, the source image has a circular object with a regular grid pattern as shown in Fig. 15(a). This object is artificially deformed in the target image by using the Corel Paintshop Pro X4 software as shown in Fig. 15(b). Fig. 15(c) shows the initial particles generated from the source shape and Fig. 15(d) shows a deformed result through a simulation using the proposed method. As shown in Fig. 15(e), our method well aligned the source circular shape into the target shape and produced similar patterns as expected.

6.2 General Observations based on Visual Assessment

For all the datasets, the liver parenchyma was modeled with about $6,500.1 \pm 3,329.2$ particles with diameter of 8 pixels and the number of boundary particles was $2,035.3 \pm 600.9$. Candidate regions of metastases were modeled with 126.4 ± 88.6 particles with the same diameter. Young's modulus for the liver parenchyma and the candidate regions of metastases were set to be 5.0×10^7 and 1.0×10^9, respectively. These values were adopted from [70] which summarized experimentally acquired Young's modulus values of the liver and other tissues. They were appropriately scaled to our simulation space of voxel unit. Poisson's ratio was set to be 0.3. Our volume-preserving deformable particle method artificially scales an individual particle to keep its volume preserved. Such individual scaling could make neighboring particles easily overlap. Combined with those overlaps, a relatively large value of Poisson's ratio, which introduces higher expelling force between overlapping particles, might result in a numerically unstable simulation. And therefore, we chose a relatively lower Poisson's ratio value than that suggested in biomechanics field [71]. The sampling distances for the signed distance field and the force field were set to be identical to the size of particle as the samplings were performed at the particle's positions during the simulation. The force field from normalized GVF was scaled up by a factor of 50.

Fig. 16 showed the subtraction artifacts and the changes in metastasis volume after applying the three registration methods of $\mathbf{NR}_{SPH}$, $\mathbf{NR}_{B-spline}$, and $\mathbf{NR}_{Proposed}$. $\mathbf{NR}_{SPH}$ registered the overall shape of liver successfully, removing the subtraction artifacts significantly. However, the position of the metastasis misaligned very much since the force applied to the boundary particles was mostly absorbed by the internal particles while they were overlapping with each other, and thus the force was not transferred to the particles representing the metastases [see Fig. 16(d)]. $\mathbf{NR}_{B-spline}$ removed most of subtraction artifacts, but the change in the metastasis volume had almost lost in the subtraction image, making the metastasis growth assessment impossible [see Fig. 16(e)]. However, the proposed method ($\mathbf{NR}_{Proposed}$) well visualized the change in metastasis volume as well as effectively removed the subtraction artifacts [see Fig. 16(f)].

6.3 Evaluation of Registration Performance

The registration accuracy was evaluated by computing the liver overlap error between the target and registered-source images. After the liver was segmented in the target and registered-source images [61], the liver overlap error was calculated by the following equation:

$$liver\_overlap\_error = \left(1 - \frac{2\left|L_T \cap L_{RS}\right|}{\left|L_T\right| + \left|L_{RS}\right|}\right) \times 100(\%), \tag{6.1}$$

where L_T and L_{RS} are the set of all voxels within the liver in the target and registered-source images, respectively, and $|L_T|$ and $|L_{RS}|$ denote the size of the sets L_T and L_{RS}.

Initial liver overlap errors between the target and source images ranged from 11.55 % to 38.73 % (mean±SD, 19.30±9.24 %). The averages and standard deviations of the liver overlap error for the three registration methods are given in Table 1. The liver overlap error increased in order of $\mathbf{NR}_{B-spline}$, $\mathbf{NR}_{Proposed}$, and $\mathbf{NR}_{SPH}$, which was consistent with the subtraction artifact results in the previous visual assessment. As $\mathbf{NR}_{B-spline}$ aligned the source image with the target image only by using the intensity difference between the two images, it effectively matched the liver, resulting in the smallest liver overlap error. In contrast, $\mathbf{NR}_{SPH}$ did not use a volume preserving constraint, and thus the particles can overlap with each other, suffering from the change of liver volume through the simulation. The repelling force in $\mathbf{NR}_{SPH}$ arising between the overlapping particles makes them restore to their original positions to some extent; however, the volume change is inevitable at any simulation instant, which introduces the severe liver overlap error. However, as $\mathbf{NR}_{Proposed}$ used volume preserving particles for the liver including the metastasis while modeling the metastasis with stiffer particles, it effectively matched the liver and preserves the metastasis in the source image as well. We measured the processing time of the proposed method on an Intel Core i5 desktop system with a 3.30 GHz processor and 8 GB of memory. The processing time, averaged over multiple tests for all the datasets, was 48.04 ± 42.52 min. We didn't impose any limitation on the number of iterations. The simulation was iterated until the distance measure of ADE converged. The number of iterations ranged from 313 to 3473 (mean ± SD, 1014 ± 898). In general, the processing time of particle based simulation method depends on the number of particles and the maximum speed of the particles. Since the proposed method computes the movement of each particle considering all the forces exerted by neighboring particles, the increase in the number of particles directly leads to the increase in the simulation time. In addition, a stiff material usually induces strong interacting force for the same amount of displacement compared to a less stiff material, resulting in faster movement of particles. To deal with those fast moving particles, a smaller time step is required for the simulation with stiffer particles, which also increases the simulation time. Therefore, the size of particles (i.e., the number of particles) and the physical properties for the material should be elaborately chosen considering the trade-off between the computational per-

Table 1: Liver Overlap Error (%)

Dataset	Initial	$\mathbf{NR}_{SPH}$	$\mathbf{NR}_{B-spline}$	$\mathbf{NR}_{Proposed}$
1	11.64	10.10	3.01	3.31
2	17.85	5.05	0.23	0.23
3	19.20	9.59	2.54	2.70
4	18.89	4.35	2.21	2.30
5	34.72	7.44	1.35	1.65
6	11.55	7.87	0.05	0.07
7	12.18	3.33	2.11	2.43
8	11.54	6.77	1.04	1.16
9	16.69	4.23	0.21	0.23
10	38.73	4.80	0.18	0.25
Average	19.30 ± 9.24	6.35 ± 2.83	1.29 ± 1.06	1.43 ± 1.15

formance and simulation accuracy.

6.4 Evaluation of Metastasis Detection Accuracy

The metastasis detection accuracy was evaluated by computing the sensitivity and specificity between the manually segmented metastases and the candidate regions of metastases which were automatically detected by intensity and sphericity analysis. An abdomen radiologist with ten years of clinical experience manually segmented metastases in the source images. For the computation of the sensitivity and specificity, true positive (TP), true negative (TN), false positive (FP), and false negative (FN) were defined as:

$$\begin{aligned} TP &= |\Omega_{Segmented} \cap \Omega_{Candidate}| \\ TN &= |(\Omega_{Liver} - \Omega_{Segmented}) \cap (\Omega_{Liver} - \Omega_{Candidate})| \\ FP &= |(\Omega_{Liver} - \Omega_{Segmented}) \cap \Omega_{Candidate}| \\ FN &= |\Omega_{Segmented} \cap (\Omega_{Liver} - \Omega_{Candidate})|, \end{aligned} \tag{6.2}$$

where $\Omega_{Segmented}$ is the set of voxels in manually segmented metastases, $\Omega_{Candidate}$ is the set of voxels in candidate regions of metastases, and Ω_{Liver} is the set of voxels in the whole liver. The sensitivity and specificity were calculated by the following equations:

$$Sensitivity = \frac{TP}{TP+FN}, Specificity = \frac{TN}{TN+FP} \tag{6.3}$$

The averages of TP, TN, FP, and FN were 2144, 551973, 11648, and 0, respectively. And the averages of sensitivity and specificity were 1.0 and 0.979, respectively. As the sensitivity of 1.0 indicated, the proposed method did NOT miss any metastasis. The FP was seemingly much greater than TP; however, the portion of metastases was very small compared to the entire volume; thus, the over-detection of metastases did not degrade the overall performance.

6.5 Evaluation of Volume Preservation

The growth estimation of metastases after the registration was evaluated by computing the volume ratio. To compute the volume ratio, the same radiologist, who segmented the metastases in the source images in section 6.4, manually segmented the metastases in the target and registered-source images. Then the metastasis volumes in the source, target, and registered-source images were measured as v_S, v_T, and v_{RS}, respectively. The volume ratios between the source and target images VR_{ST}, between the registered-source and source images VR_{RS}, and between the registered-source and target images VR_{RT} were calculated as $VR_{ST} = v_S/v_T$, $VR_{RS} = v_{RS}/v_S$, and $VR_{RT} = v_{RS}/v_T$, respectively. The metastasis volume in the source image was completely preserved through the registration if $VR_{RS} = 1.0$ (ideal case), compressed if $VR_{RS} < 1.0$, and expanded if $VR_{RS} > 1.0$. And if VR_{RT} is identical to VR_{ST}, the growth of metastases is accurately estimated after registration.

The geometric means and standard deviations of those volume ratios for the three registration methods were presented in Table 2. $\mathbf{NR}_{Proposed}$, which applies a sort of incompressibility constraint to the metastases by modeling them with stiffer particles having higher Young's modulus, exhibited VR_{RS} close to 1.0, indicating that they preserved the metastases almost completely. However, $\mathbf{NR}_{SPH}$ and $\mathbf{NR}_{B-Spline}$, which do not use the incom-

Table 2: Evaluation Results Of Metastasis Volume Change

	VR_{RS}	VR_{ST}	VR_{RT}
$\mathbf{NR}_{SPH}$	1.30 x/ 1.10	0.63 x/ 1.60	0.82 x/ 1.56
$\mathbf{NR}_{B-spline}$	1.29 x/ 1.09	0.63 x/ 1.60	0.81 x/ 1.59
$\mathbf{NR}_{Proposed}$	1.08 x/ 1.07	0.63 x/ 1.60	0.68 x/ 1.62

pressibility constraint, showed VR_{RS} much higher than 1.0 (1.30 and 1.29, 30.4 % and 28.9 % of volume expansion), indicating that they both inappropriately expanded the metastases.

As shown in Table 2, $\mathbf{NR}_{Proposed}$ which applies a sort of incompressibility constraint in the non-rigid registration step, exhibited VR_{RT} very close to VR_{ST}, indicating that they accurately estimated the metastasis growth after the registration. However, $\mathbf{NR}_{SPH}$ and $\mathbf{NR}_{B-Spline}$ showed VR_{RT} much higher than VR_{ST}, indicating that it failed to accurately estimate the metastasis growth by making the metastases in the source image inappropriately similar to those in the target image.

6.6 Parameter Study

As discussed earlier in section 6.3, the particle size affects the computational performance and simulation accuracy. Table 3 the simulation time and the registration accuracy with varying particle size. As shown in Table 3, the smaller becomes the particle size, the greater becomes the simulation time. Using particles of smaller size, more particles are needed to fill the

Table 3: Performance Test Results with Varying Particle Size

Particle size (voxels)	Number of particles	Runtime (min)	Liver overlap error (%)	VR_{RS}
16	590	6.05	2.48	1.02
8	5873	26.12	1.42	1.03
4	45450	391.53	1.41	1.04
2	369018	6942.81	1.38	1.05

same volume, resulting in the increase of the number of particles. During the simulation, the interacting forces should be computed for all pairs of particles, the overall computation time should increase with the increased number of particles. For the particle sizes 16, 8, 4 and 2, timesteps were 0.0042, 0.0021, 0.0010 and 0.0005 seconds, respectively. The runtime in table 3 shows the actual time consumed for the same period of simulation time(i.e., 1 second).

With the smaller particle size, the registration accuracy of liver overlap error gets improved because the sampling distance of the distance measure decreases accordingly (Table 3). The final distance measures were 3.96, 2.50, 1.35 and 1.13 mm respectively. However, that improvement is not so apparent, seemingly saturated, when the particle size gets smaller than 8. It might be attributed to it that the same volume of metastasis was modeled with more particles and their compression or expansion through the simulation causes volume changes in an unexpected way. In other words, particles with smaller size fits the source shape to the target shape more tightly, but

Table 4: Registration Performance Test with Varying Poisson's Ratio

Poisson's ratio	Liver overlap error	Cancer volume ratio
0.3	1.422	1.029
0.4	1.353	1.028
0.41	1.333	1.021
0.42	1.401	1.025
0.43	1.445	1.034
0.45	1.738	1.024

the internal part of the shape could be deformed undesirably, hindering the volume preservation. Therefore, we chose 8 for the particle size considering both the computation time and the registration accuracy.

Even though we used 0.3 for Poisson's ratio in all our experiemtns for the numerial stability and to simulate all the datasets in same condition, we also experiemted the effect of changing Poisson's ratio for a dataset. Poisson's ratio is the ratio of the fraction (or percent) of expansion divided by the fraction (or percent) of compression, for small values of these changes. Most materials have Poisson's ratio values ranging between 0.0 and 0.5 and a perfectly incompressible material deformed elastically would have a Poisson's ratio of exactly 0.5. However, as Poisson's ratio approaches 0.5, some terms in the stress-strain relationship approach infinity and it cannot be handled. Table 4 shows changes of liver over error (LOE) and cancer volume ratio (CVR) with varying Poisson's ratio. The registration accury increases with higher Poisson's ratio, however, it again decreases for the Poisson's ratio higher than 0.41. Since our method emulates the Poisson effect by deforming particles and the maximum stable value of Poisson's ratio changes for each dataset, we set 0.3 to Poisson's ratio in the experiments.

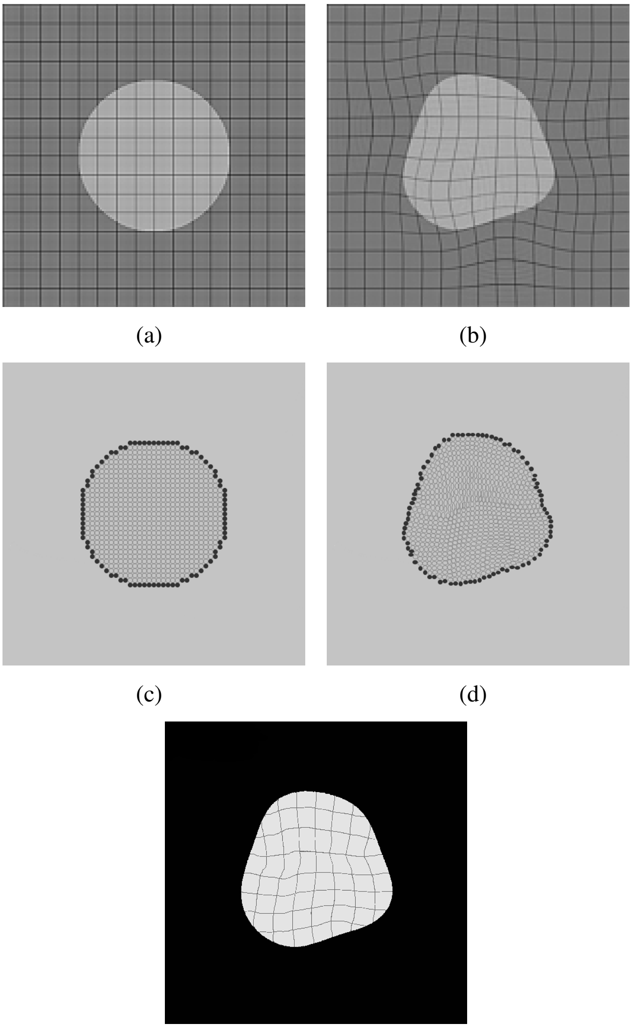

(a) (b) (c) (d) (e)

Figure 15: 2D deformation of a circular object. (a) Source image with a circular object in a regular grid pattern. (b) Target image obtained by artificially deforming the source image using Corel Paintshop Pro X4 software. (c) Particles placed in the source shape of the circular object in (a). (d) Deformed particles using the proposed method. (e) Final deformed image.

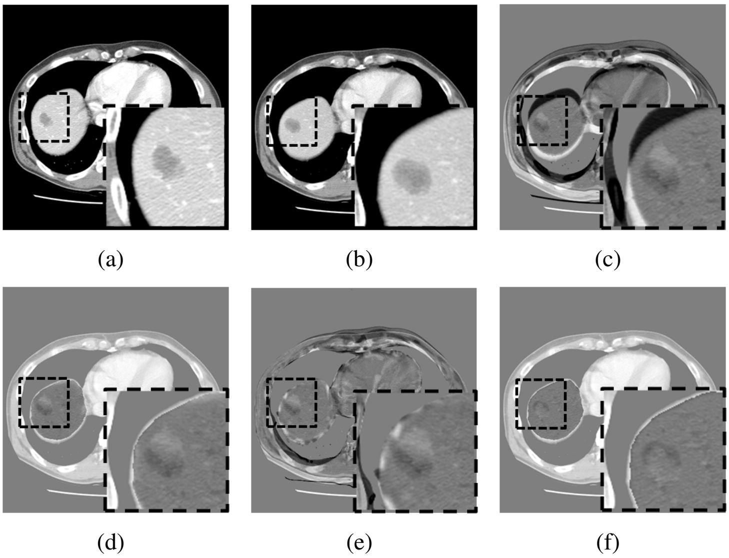

Figure 16: Comparison of $\mathbf{NR}_{SPH}$, $\mathbf{NR}_{B-spline}$ [1, 2], and $\mathbf{NR}_{Proposed}$ for a slice taken from CT scans with noticeable metastasis changes. The metastasis is enclosed by the dotted rectangle. (a) and (b) are CT slice images taken at times t_0 (source image) and t_1 (target image), respectively. (c) is a subtraction image between the source and target images before registration. (d)-(f) are subtraction images between the target image and the registered-source image with $\mathbf{NR}_{SPH}$, $\mathbf{NR}_{B-spline}$ [1, 2], and $\mathbf{NR}_{Proposed}$, respectively.

Chapter 7

Conclusion

This paper presented a novel physically based non-rigid registration method based on SPH for the hepatic metastasis volume-preserving registration between follow-up liver CT images. First, we automatically detect the liver and candidate regions of metastases. Subsequently, we conduct rigid registration for global image matching, which serves as an initial estimate for the following non-rigid registration. Then, we perform a physically based non-rigid registration for local matching based on SPH. Particles are placed in the source shape (i.e., liver in the source image) and move along GVF-based force field to fit into the target shape (i.e., liver in the target image). In this non-rigid registration, the interaction between particles is handled by a novel deformable particle method which is proposed to preserve the volume of metastases during the registration. The experimental results demonstrated that the proposed method almost perfectly preserves the metastases in the source image as well as effectively matches the liver between the source and target images, enabling the accurate assessment of the volume change of the metastases. It is expected that the proposed method delivers a substantial aid in measuring the size change of index lesion (i.e., metastasis) after the chemotheraphy of metastasis patients in radiation oncology.

Unlike conventional non-rigid registration approaches which deform images based on intensity-relevant information such as intensity and gradient, our method models the liver and metastasis as a set of particles with their own elastic properties. By exploiting the fact that the metastases are stiffer than other normal cells in the liver parenchyma, the metastasis candidate regions are filled with particles with higher stiffness (e.g. higher Young's modulus). In addition, the particles are physically interacted and deformed using a new deformable particle method which is proposed with intent to preserve the metastasis to the best. In this way, our method improves the overall registration accuracy and the metastasis volume preservation. Furthermore, since each particle can carry its intrinsic physical properties during the registration, various organs in human body with partially varying physical properties (e.g. stiffness, viscosity, and density) could be simulated successfully.

In this dissertation, we classify the candidate regions of metastases by considering both the intensity and sphericity values. In future work, we are planning to improve our classification method by using texture analysis (e.g. gray-level cooccurrence matrix) so that the candidate regions are further minimized. In addition, the proposed method could not be successfully applied to some datasets in which the topologies of liver changes between the source and target images. This was resulted from inconsistent segmentation of liver regions because some part of liver directly contacts other organs making it hard to distinguish the liver from other organs. In simulation, this makes particles at boundary interact with other boundary particles which were not neighbors at initial stage. Therefore, interactions between particles not connected by linear elasticity should be handled in the future. Regarding the computational performance, even though current advances in computing hardware has enabled us to use particle-based physical simulation for various applications, it still requires much higher computation than image-based approaches. Thus, we are planning to further optimize and accelerate the proposed method using a parallel computing architecture such as CUDA (compute unified device architecture) to make it more appropriate for clinical uses.

Bibliography

[1] S. Park, B. H. Kim, J. Lee, J. M. Goo, and Y.-G. Shin, "GGO nodule volume-preserving nonrigid lung registration using GLCM texture analysis.," *IEEE Trans. Biomed. Eng.*, vol. 58, no. 10, pp. 2885–2894, 2011.

[2] D. Rueckert, L. I. Sonoda, C. Hayes, D. L. G. Hill, M. O. Leach, and D. J. Hawkes, "Nonrigid registration using free-form deformations: Application to breast MR images," *IEEE Trans. Med. Imag.*, vol. 18, no. 8, pp. 712–721, 1999.

[3] K. W. Kim, J. M. Lee, E. Klotz, H. S. Park, D. H. Lee, J. Y. Kim, S. J. Kim, S. H. Kim, J. Y. Lee, J. K. Han, and B. I. Choi, "Quantitative CT color mapping of the arterial enhancement fraction of the liver to detect hepatocellular carcinoma," *Radiology*, vol. 250, no. 2, pp. 425–434, 2009.

[4] Y. Masutani, K. Uozumi, M. Akahane, and K. Ohtomo, "Liver CT image processing: A short introduction of the technical elements," *Eur. J. Radiol.*, vol. 58, no. 2, pp. 246–251, 2006.

[5] S. Emelianov, J. Rubin, M. Lubinski, A. Skovoroda, and M. O'Donnell, "Elasticity imaging of the liver: Is a hemangioma hard or soft?," in *Proc. of Ultrason. Symp.*, vol. 2, pp. 1749–1752, 1998.

[6] W.-C. Yeh, P.-C. Li, Y.-M. Jeng, H.-C. Hsu, P.-L. Kuo, M.-L. Li, P.-M. Yang, and P.-H. Lee, “Elastic modulus measurements of human liver and correlation with pathology,” *Ultrasound Med. Biol.*, vol. 28, no. 4, pp. 467–474, 2002.

[7] H. M. Yin, L. Z. Sun, G. Wang, and M. W. Vannier, “Modeling of elastic modulus evolution of cirrhotic human liver,” *IEEE Trans. Biomed. Eng.*, vol. 51, no. 10, pp. 1854–1856, 2004.

[8] A. Charnoz, V. Agnus, and L. Soler, “Portal vein registration for the follow–up of hepatic tumours,” *Lect. Notes Comput. Sci.*, vol. 3216, pp. 878–886, 2004.

[9] A. Charnoz, V. Agnus, G. Malandain, C. Forest, M. Tajine, and L. Soler, “Liver registration for the follow-up of hepatic tumors,” *Lect. Notes Comput. Sci.*, vol. 3750, pp. 155–162, 2005.

[10] E. Okumura, S. Sanada, M. Suzuki, and O. Matsui, “A computer-aided temporal and dynamic subtraction technique of the liver for detection of small hepatocellular carcinomas on abdominal CT images,” *Phys. Med. Biol.*, vol. 51, no. 19, pp. 4759–4771, 2006.

[11] C. Fujioka, J. Horiguchi, M. Ishifuro, H. Kakizawa, M. Kiguchi, N. Matsuura, M. Hieda, T. Tachikake, F. Alam, T. Furukawa, and K. Ito, “A feasibility study: Evaluation of radiofrequency ablation therapy to hepatocellular carcinoma using image registration of preoperative and postoperative CT,” *Acad. Radiol.*, vol. 13, no. 8, pp. 986–94, 2006.

[12] J. Hajnal, D. Hawkes, and D. Hill, *Medical Image Registration*. Biomedical Engineering Series, CRC Press, 2001.

[13] J. Maintz and M. Viergever, "A survey of medical image registration," *Medical Image Analysis*, vol. 2, no. 1, pp. 1–36, 1998.

[14] M. Holden, "A review of geometric transformations for nonrigid body registration," *IEEE Trans. Med. Imaging*, vol. 27, no. 1, pp. 111–128, 2008.

[15] D. Rueckert and P. Aljabar, "Nonrigid Registration of Medical Images: Theory, Methods, and Applications," *IEEE Signal Processing Magazine*, vol. 27, pp. 113–119, July 2010.

[16] R. Y. Tsai, "A versatile camera calibration technique for high-accuracy 3d machine vision metrology using off-the-shelf tv cameras and lenses," *IEEE Journal on Robotics and Automation*, vol. 3, pp. 323–344, 1987.

[17] J. Duchon, "Interpolation des fonctions de deux variables suivant le principe de la flexion des plaques minces," *ESAIM: Mathematical Modelling and Numerical Analysis - Modélisation Mathématique et Analyse Numérique*, vol. 10, no. R3, pp. 5–12, 1976.

[18] J. Meinguet, "Multivariate interpolation at arbitrary points made simple," *JApplMathPhys*, vol. 30, no. 2, pp. 292–304, 1979.

[19] F. L. Bookstein, “Shape and the information in medical images: A decade of the morphometric synthesis,” *Computer Vision and Image Understanding*, vol. 66, no. 2, pp. 97–118, 1997.

[20] M. Fornefett, K. Rohr, H. S. Stiehl, and A. K. Systeme, “Radial basis functions with compact support for elastic registration of medical images,” *IVC*, vol. 19, pp. 1–2, 1999.

[21] A. Goshtasby, *2-D and 3-D Image Registration: For Medical, Remote Sensing, and Industrial Applications*. John Wiley & Sons, 2005.

[22] T. W. Sederberg and S. R. Parry, “Free-form deformation of solid geometric models,” in *Proceedings of the 13st Annual Conference on Computer Graphics and Interactive Techniques, SIGGRAPH 1986*, pp. 151–160, 1986.

[23] S. Lee, G. Wolberg, K.-Y. Chwa, and S. Y. Shin, “Image metamorphosis with scattered feature constraints,” *IEEE Trans. Vis. Comput. Graph.*, vol. 2, no. 4, pp. 337–354, 1996.

[24] S. Lee, G. Wolberg, and S. Y. Shin, “Scattered data interpolation with multilevel b-splines,” *IEEE Trans. Vis. Comput. Graph.*, vol. 3, no. 3, pp. 228–244, 1997.

[25] D. Rueckert, C. Hayes, C. Studholme, P. E. Summers, M. O. Leach, and D. J. Hawkes, “Non-rigid registration of breast mr images using mutual information,” in *MICCAI*, pp. 1144–1152, 1998.

[26] R. Bajcsy and S. Kovačič, "Multiresolution elastic matching," *Comput. Vision Graph. Image Process.*, vol. 46, no. 1, pp. 1–21, 1989.

[27] C. Davatzikos, "Spatial transformation and registration of brain images using elastically deformable models," *Comput. Vis. Imag. Underst.*, vol. 66, no. 2, pp. 207–222, 1997.

[28] G. E. Christensen, R. D. Rabbitt, and M. I. Miller, "Deformable templates using large deformation kinematics," *IEEE Trans. Imag. Process.*, vol. 5, no. 10, pp. 1435–1447, 1996.

[29] H. Lester, "A survey of hierarchical non-linear medical image registration," *Pattern Recognition*, vol. 32, pp. 129–149, Jan. 1999.

[30] A. Roche, G. Malandain, X. Pennec, and N. Ayache, "The correlation ratio as a new similarity measure for multimodal image registration," in *MICCAI*, pp. 1115–1124, 1998.

[31] C. E. Shannon, "A mathematical theory of communication," *The Bell System Technical Journal*, vol. 27, pp. 379–423, 623–656, July, October 1948.

[32] J. P. W. Pluim, J. B. A. Maintz, and M. A. Viergever, "Mutual information based registration of medical images: A survey," *IEEE Trans. Med. Imaging*, vol. 22, no. 8, pp. 986–1004, 2003.

[33] F. Maes, A. Collignon, D. Vandermeulen, G. Marchal, and P. Suetens, "Multimodality image registration by maximization of mutual information," *IEEE Trans. Med. Imaging*, vol. 16, no. 2, pp. 187–198, 1997.

[34] P. A. Viola and W. M. W. III, "Alignment by maximization of mutual information," *International Journal of Computer Vision*, vol. 24, no. 2, pp. 137–154, 1997.

[35] C. Studholme, D. L. G. Hill, and D. J. Hawkes, "An overlap invariant entropy measure of 3d medical image alignment," *Pattern Recognition*, vol. 32, no. 1, pp. 71–86, 1999.

[36] F. Maes, D. Vandermeulen, and P. Suetens, "Comparative evaluation of multiresolution optimization strategies for multimodality image registration by maximization of mutual information," *Medical Image Analysis*, vol. 3, no. 4, pp. 373–386, 1999.

[37] S. Klein, M. Staring, and J. P. W. Pluim, "Evaluation of optimization methods for nonrigid medical image registration using mutual information and b-splines," *IEEE Transactions on Image Processing*, vol. 16, no. 12, pp. 2879–2890, 2007.

[38] C. Broit, *Optimal Registration of Deformed Images*. Doctoral dissertation, University of Pennsylvania, 1981.

[39] G. Wollny and F. Kruggel, "Computational cost of nonrigid registration algorithms based on fluid dynamics," *IEEE Trans. Med. Imag.*, vol. 21, no. 8, pp. 946–952, 2002.

[40] R. M. Koch, S. H. M. Roth, M. H. Gross, A. P. Zimmermann, and H. F. Sailer, "A framework for facial surgery simulation," in *Proc. of the 18th Spring Conference on Computer Graphics*, SCCG '02, (New York, NY, USA), pp. 33–42, ACM, 2002.

[41] S. E. Hieber and P. Koumoutsakos, “A lagrangian particle method for the simulation of linear and nonlinear elastic models of soft tissue,” *J. Comput. Phys.*, vol. 227, no. 21, pp. 9195–9215, 2008.

[42] M. Bro-nielsen and C. Gramkow, “Fast fluid registration of medical images,” in *Proc. of Visualization in Biomedical Computing*, pp. 267–276, 1996.

[43] C. Davatzikos, J. L. Prince, and R. N. Bryan, “Image registration based on boundary mapping,” *IEEE Trans. Med. Imag.*, vol. 15, no. 1, pp. 112–115, 1996.

[44] R.A. Gingold and J.J. Monaghan, “Smoothed particle hydrodynamics - theory and application to non-spherical stars,” *Mon. Not. Roy. Astron. Soc.*, vol. 181, pp. 375–389, Nov 1977.

[45] L. Lucy, “A numerical approach to the testing of the fission hypothesis,” *Astron. J.*, vol. 82, pp. 1013–1024, Dec 1977.

[46] G. R. Liu and M. B. Liu, *Smoothed particle hydrodynamics: a meshfree particle method.* World Scientific Publishing, 2003.

[47] J. J. Monaghan, “Smoothed particle hydrodynamics,” *Rep. Progr. Phys.*, vol. 68, no. 8, pp. 1703–1759, 2005.

[48] B. Adams and M. Wicke, “Meshless approximation methods and applications in physics based modeling and animation,” in *Eurographics 2009 Tutorials*, pp. 213–239, 2009.

[49] J. J. Monaghan and J. C. Lattanzio, “A refined particle method for astrophysical problems,” *Astronomy and Astrophysics*, vol. 149, pp. 135–143, Aug. 1985.

[50] J. P. Morris, “A study of the stability properties of smooth particle hydrodynamics,” *Publications Astronomical Society of Australia*, vol. 13, no. 1, pp. 97–102, 1996.

[51] J. Morris, *Analysis of Smoothed Particle Hydrodynamics with Applications*. PhD thesis, Monash University, 1996.

[52] J. J. Monaghan, “Simulating free surface flows with sph,” *J. Comput. Phys.*, vol. 110, no. 2, pp. 543–574, 1992.

[53] J. J. Monaghan, “Smoothed particle hydrodynamics,” *Annu. Rev. Astron. Astr.*, vol. 30, no. 2, pp. 399–406, 1994.

[54] P. W. Cleary, “Modelling confined multi-material heat and mass flows using SPH,” *App. Math. Modelling*, vol. 22, pp. 981–993, 1998.

[55] M. Desbrun and M. paule Gascuel, “Smoothed particles: A new paradigm for animating highly deformable bodies,” in *Proc. of EG Workshop on Computer Animation and Simulation*, pp. 61–76, 1996.

[56] M. Müller, R. Keiser, A. Nealen, M. Pauly, M. Gross, and M. Alexa, “Point based animation of elastic, plastic and melting objects,” in *Proc. of the ACM SIGGRAPH/EUROGRAPHICS Symposium on Computer Animation*, pp. 141–151, 2004.

[57] B. Solenthaler, J. Schlafli, and R. Pajarola, “A unified particle model for fluid solid interactions,” *Comput. Animat. Virtual Worlds*, vol. 18, no. 1, pp. 69–82, 2007.

[58] M. Becker, M. Ihmsen, and M. Teschner, “Corotated SPH for deformable solids,” in *Proc. of Eurographics Workshop on Natural Phenomena*, pp. 27–34, 2009.

[59] M. Müller, B. Heidelberger, M. Teschner, and M. Gross, “Meshless deformations based on shape matching,” *ACM Trans. Graph.*, vol. 24, no. 3, pp. 471–478, 2005.

[60] R. Schmedding and M. Teschner, “Inversion handling for stable deformable modeling,” *Vis. Comput.*, vol. 24, no. 7, pp. 625–633, 2008.

[61] J. Lee, N. Kim, H. Lee, J. B. Seo, H. J. Won, Y. M. Shin, Y. G. Shin, and S.-H. Kim, “Efficient liver segmentation using a level-set method with optimal detection of the initial liver boundary from level-set speed images,” *Comput. Meth. Programs Biomed.*, vol. 88, no. 1, pp. 26–38, 2007.

[62] J. Stawiaski, E. Decenciere, and F. Bidault, “Interactive liver tumor segmentation using graph-cuts and watershed,” in *Proc. of Workshop on 3D Segmentation in the Clinic: a Grand Challenge II. Liver Tumor Segmentation Challenge*, MICCAI’08, 2008.

[63] M. Freiman, O. Eliassaf, Y. Taieb, L. Joskowicz, and J. Sosna, “A bayesian approach for liver analysis: Algorithm and validation study,” *Lect. Notes Comput. Sci.*, vol. 5241, pp. 85–92, 2008.

[64] F. Chang, C. jen Chen, and C. jen Lu, “A linear-time component-labeling algorithm using contour tracing technique,” *Comput. Vis. Imag. Underst.*, vol. 93, no. 2, pp. 206–220, 2004.

[65] C. Xu and J. L. Prince, “Gradient vector flow: A new external force for snakes,” in *Proc. of IEEE Conf. on Comp. Vis. Patt. Recog.*, pp. 66–71, 1997.

[66] M. Akmal Butt and P. Maragos, “Optimum design of chamfer distance transforms,” *IEEE Trans. Imag. Process.*, vol. 7, no. 10, pp. 1477–1484, 1998.

[67] S. Raya and J. Udupa, “Shape-based interpolation of multidimensional objects,” *IEEE Trans. Med. Imag.*, vol. 9, no. 1, pp. 32 –42, 1990.

[68] B. Adams, M. Pauly, R. Keiser, and L. J. Guibas, “Adaptively sampled particle fluids,” *ACM Trans. Graph.*, vol. 26, no. 3, 2007.

[69] J. P. Gray, J. J. Monaghan, and R. P. Swift, “SPH elastic dynamics,” *Computer methods in applied mechanics and engineering*, vol. 190, pp. 6641–6662, 2001.

[70] P. N. T. Wells and H.-D. Liang, “Medical ultrasound: Imaging of soft tissue strain and elasticity,” *J. R. Soc. Interface*, vol. 43, no. 64, pp. 1521–1549, 2011.

[71] Y. C. Fung, *Biomechanics : Mechanical properties of living tissues*. New York: Springer-Verlag, 1981.

초 록

최근 컴퓨팅 하드웨어의 발달은 정확도 향상을 위해 물리 기반의 시뮬레이션 기술을 다양한 연구 분야에 적용할 수 있게 하였다. 본 논문에서는 입자를 이용하여 시뮬레이션하는 방법 중 하나인 입자 보간 방식의 유체역학 (smoothed particle hydrodynamics) 기술을 이용하여, 후속 컴퓨터 단층촬영 영상(computed tomography) 사이에 간전이(hepatic metastasis) 체적을 보전하는 물리 기반의 비정형체 정합 기술을 제안한다. 제안 방법은 간과 간전이를 물리적 속성을 동반하는 일련의 입자로 표현하며, 간전이가 정상 간에 비해 강한 탄성을 보인다는 사실에 기반하여 간전이로 짐작되는 부위를 상대적으로 강한 탄성을 갖는 입자로 표현하였다. 초기에 간과 간전이 후보 영역을 나타내는 입자들은 입력 영상의 해당 영역에 위치되며, 정합하고자 하는 대상 영상으로 부터 경사도 벡터 흐름(gradient vector flow) 방법으로 계산된 힘의 장을 따라 이동된다. 이 때, 각 입자는 간전이의 체적을 최대한 보존하기 위해 제안된 변형 가능 입자 방식에 따라 서로 물리적으로 상호작용하며 변형된다. 10명의 환자 데이터를 이용한 실험 결과에 따르면, 후속 컴퓨터 단층촬영 (CT) 영상 간의 정합 과정에서 간의 모양을 효과적으로 일치시킬 뿐만 아니라 간전이의 체적을 거의 완벽하게 보존하여 간전이의 체적 변화를 정확하게 진단할 수 있게 하였다. 이 결과는 간전이 환자가 화학 요법을 시행 한 후 암의 진행 상태를 판단하기 위해 간전이의 크기 변화를 측정하는데 도움을 줄 수 있는 방법임을 시사한다.

키워드: 컴퓨터 단층촬영, 간전이, 체적 보존 입자 방식, 컴퓨터 시뮬레이션, 입자 보간 방식 유체역학

학번: 99325-811